Evolution of structural, electronic and magnetic properties upon Mg-doping in BaIrO$_3$

A Thesis

submitted to

Indian Institute of Science Education and Research Pune
in partial fulfillment of the requirements for the
BS-MS Dual Degree Programme

by

Dubbaku Sri Pragna

Indian Institute of Science Education and Research Pune
Dr. Homi Bhabha Road,
Pashan, Pune 411008, INDIA.

April, 2020

Supervisor: Dr. Surjeet Singh

© Dubbaku Sri Pragna 2020

Certificate

This is to certify that this dissertation entitled Evolution of structural, electronic and magnetic properties upon Mg-doping in $BaIrO_3$ towards the partial fulfilment of the BS-MS dual degree programme at the Indian Institute of Science Education and Research, Pune represents study/work carried out by Dubbaku Sri Pragnaat Indian Institute of Science Education and Research under the supervision of Dr. Surjeet Singh, Department of Physics, during the academic year 2019-2020.

Dubbaku Sri Pragna

Dr. Surjeet Singh 12.4.20

This thesis is dedicated to my mother, Vijaya Kumari for her unconditional love and emotional support throughout this journey.

Declaration

I hereby declare that the matter embodied in the report entitled Evolution of structural, electronic and magnetic properties upon Mg-doping in $BaIrO_3$ are the results of the work carried out by me at the Department of Physics, Indian Institute of Science Education and Research, Pune, under the supervision of Dr. Surjeet Singh and the same has not been submitted elsewhere for any other degree.

Dubbaku Sri Pragna

Dr.Surjeet Singh

12.4.20

Acknowledgments

I sincerely thank my project supervisor Dr.Surjeet Singh for allowing me to work on this project. I am immensely grateful for his constant support and guidance throughout the project. His enthusiasm towards research and periodic discussions has always motivated me and helped in my improvement.

I want to thank my lab members, firstly Prachi Telang, for training me in the primary usage of lab equipment and for taking out time for discussions amid her busy schedule. I also thank Dibyata and Anupam for helping me in PPMS measurements and for helpful discussions; Saurabh Kumar, Navita, and Prakash for helping me in every way possible within their reach in times of need; Ankit Kumar for insightful discussions regarding Raman spectroscopy; Nashra, Sagar and Nupur for helping me in one way or the other. The much-needed tea breaks with you people were something that I always look forward to because of all the funny banters, serious discussions regarding anything and everything that were elements of an energy boost mentally.

I extend my gratitude to Anil Sir and Sudhir Sir for FESEM measurements, Dr. Nirmalya Ballav for Raman measurements. I thank IISER-PUNE for such a healthy atmosphere and high-end lab facilities to work.

I must thank my friends Shivani, Sreelakshmi and Anwesha who has always been there to lift my spirits when I am low and who would never forget to check on me every single day; Shephali who brings out my crazy version; Shreya with whom I can hold meaningful conversations about anything under the sun. Weekend dinners, 2 a.m discussions, trouble sharings, in-depth life talks, every moment with you guys will be cherished for a lifetime. Last but not least,I express my heartfelt gratitude to my parents and my sister for their incredible support and for always believing in me.

x

Abstract

In last five years or so, correlated topological materials have attracted enormous attention. In these materials, the interplay between electronic correlations, spin-orbit coupling, and crystal field effect gives rise to unconventional "correlated topological phases," such as spin-orbit assisted Mott insulator, Weyl semimetal, Axion insulator and a plethora of quantum spin liquids, that are a subject of significant contemporary interest.

In this work, we investigate a perovskite iridate, $BaIrO_3$, which is a candidate correlated topological material. It shows a concomitant ferromagnetic and charge density wave (CDW) ordering at ($T_c \sim 180$ K) along with an insulating ground state. $BaIrO_3$ has a very sensitive structural and physical properties dependence on pressure. We synthesized Mg-doped samples: $Ba_{1-x} Mg_x IrO_3$ (x = 0, 0.05, 0.1) and $BaIr_{1-x}Mg_x O_3$ (x = 0.05, 0.1, 0.15, 0.2, 0.3, 0.33) using the conventional solid-state reaction method. We obtained several single-phase samples either crystallizing with the 9R structure of $BaIrO_3$ having a monoclinic symmetry, or with a hexagonal triple perovskite structure of $Ba_3MgIr_2O_9$. The electronic and magnetic properties of single-phase samples has been studied. We show that up to 5% of Mg doping, the 9R structure remains stable, the electrical conductivity increases significantly and the magnitude of magnetic susceptibility decreases, but the magnetic ordering temperature remains unchanged, which suggests that the Ir-Ir exchange interaction remains nearly unchanged upon Mg doping but the ordered Ir moment weakens. The sample $Ba_3MgIr_2O_9$, shows a paramagnetic susceptibility with no magnetic transition down to the lowest measurement temperature.

Contents

List of Figures

List of Tables

Chapter 1

Introduction

Transition metal oxides (TMOs) are an extensively studied class of solids varying from simple binary oxides to complex ternary, quaternary or higher oxides, because of the wide variety of structures and properties they exhibit. For many decades most of the research was devoted to compounds derived from 3d transition metals as one of the constituents. Some of the revolutionary discoveries in 3d-perovskite oxides include high-temperature superconductivity in cuprates ($YBa_2Cu_3O_7$) [1], colossal magneto-resistance in manganites ($La_{0.67}Mn_{0.33}O_3$), [2] etc. These discoveries not only gave a breakthrough in research of perovskite related structures but also found several practical applications in the field of medical diagnostics and data storage devices. On the other hand, very little attention has been given to 5d TMOs in terms of this basic and applied research which can be ascribed to less abundance and production costs of these elements [3]. However, lately, much interest has been invigorated in the 5d TMOs as they exhibit various exotic physical phenomena that are contrasting to their 3d analogs. Due to the diffuse nature of 5d- orbitals, the electron-electron correlations (U) decrease in the 5d series. As U reduces, electrons in the system become more delocalised; hence the 5d TMOs are expected to be metallic, but most of them are insulators defying intuitive expectations. Early experimental observations in Sr_2IrO_4, $Sr_3Ir_2O_7$ exemplify this behaviour [4]. The 5d TMOs have emerged as a prototype materials where topology of electronic structure and strong electronic correlations come hand-in-hand. In 5d TMOs, electron-electron correlations (U), spin-orbit coupling (SOC, λ) and crystal field effect (Δ) act at comparable energy scales [5]. The interplay of these interactions which are at close correspondence results in a range of unconventional "correlated topological phases" such as spin-orbit induced

Mott insulator, Weyl semimetal, quantum spin liquid, superconductivity, topological insulators, etc. A brief description of these interactions is given in further sections. Various exotic quantum phases that can be observed depending on the competition/cooperation of U and SOC; are given in Fig. 1.1. taken from [6].
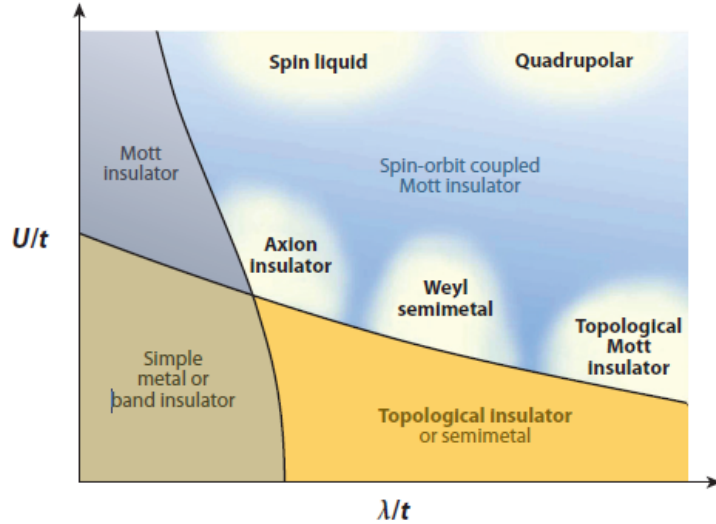
Figure 1.1: Schematic diagram of various quantum phases depending on the strengths of various interactions. Here t is the hopping integral.

Among the 5d TMOs, iridates with Ir in a 4+ valence state (i.e., $5d^5$ configuration) are the ones that have generated a major interest within the condensed matter community. The radical departure from the conventional intuitions of 5d TMOs was first observed in iridium based oxides. The emergent field of strongly correlated electron physics combined with strong SOC started with the study of Sr_2IrO_4 and Sr_2RuO_4. Their structural similarity with the most celebrated parent compound of cuprate superconductors, La_2CuO_4, has motivated to study these compounds. While superconductivity was discovered in Sr_2RuO_4, an insulating antiferromagnetic ground state was found in Sr_2IrO_4. Kim et al. in 2008 proposed the strong SOC as a possible candidate responsible for this unconventional observation. An octahedral crystal field splits the 5d-orbitals of Ir^{4+} into doubly degenerate, e_g and triply degenerate, t_{2g} orbitals. The t_{2g} band is further split by strong spin-orbit coupling into doubly degenerate fully-filed ground state ($J_{eff} = 3/2$) and half-filled excited doublet state ($J_{eff} = 1/2$). The same is depicted in Fig. 1.2. Since $J_{eff} = 1/2$ is a very narrow band, moderate U combined with strong SOC opens an energy gap leading to a spin-orbit driven $J_{eff} = 1/2$ Mott insulating state [7]. The realization of $J_{eff} = 1/2$ state is an ardent manifestation of the delicate interplay of

interactions stated earlier. Since this intriguing observation, an extensive research has been done on Sr_2IrO_4. $Sr_3Ir_2O_7$, $SrIrO_3$, $BaIrO_3$, Ba_2IrO_4 are some of the examples of $J_{eff} = 1/2$ state [8], [9], [10], [11].
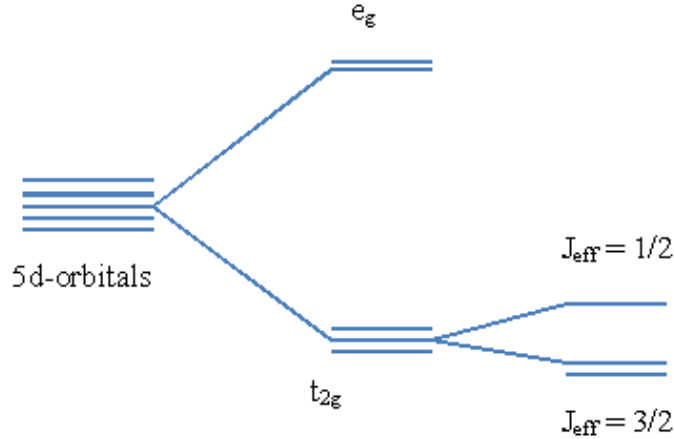
Figure 1.2: Crystal field splitting in iridates

Since the realization of the importance of spin-orbit coupling in Sr_2IrO_4, iridates have been characteristic materials for studying the interplay of SOC and electron-electron correlations. Among perovskite iridates, a subfamily, "113" alkaline-earth iridates, $AIrO_3$ (A = Ca, Sr, Ba), are of profound interest. This family of compounds is subjected to relatively few studies, given their harsh synthesis conditions and structural variations. For example, theoretical calculations predict a topological semimetal state in orthorhombic perovskite (Pv) $SrIrO_3$. However, it is challenging to stabilise this phase at ambient conditions. It is synthesized under high pressure and high-temperature conditions (2GPa,1650°C). The ambient phase of $SrIrO_3$, on the other hand, adopts a monoclinically distorted hexagonal (6H) structure, exhibiting properties different from the high-pressure phase [11]. $CaIrO_3$ has two structural polymorphs, namely post-perovskite (pPv) and perovskite structures [12], [13]. In the case of $BaIrO_3$, four structural polymorphs are possible; 9R, 5H, 6H, and 3C depending on synthesis conditions [See Table 1.1]. The general trend observed in high-pressure synthesis among TMOs is 2H-9R-4H-6H-3C. In $BaIrO_3$, a new high-pressure polytype, 5H is observed in a narrow pressure range. Each of these polymorphs has interesting properties of

their own, thus exhibiting an intimate structure-property relationship [14], [15], [17].

S. No.	Polytype	Pressure range	Crystal Structure
1	9R	3GPa	Monoclinic (C2/m)
2	5H	4GPa	Monoclinic (C2/m)
3	6H	5GPA-18GPa	Monoclinic (C2/c)
4	3C	25GPa	Tetragonal ($I4$/mcm)

Table 1.1: High-pressure polytypes of $BaIrO_3$

1.1 Motivation

$BaIrO_3$ stands out from most of the other systems because of several unique features such as high magnetic ordering temperature with small magnetic moment, an insulating ground state, simultaneous ferromagnetic and charge density wave (CDW) ordering near 180K, and, non-ohmic behaviour. [18],[19]. Small perturbations like doping, pressure and temperature can tip the balance between the interactions in this system resulting in changes in electronic and magnetic properties. Various studies reveal that doping at Ba and Ir sites results in the occurrence of several structural transitions along with changes in magnetic and electrical properties. Dilute doping of Sr at Ba site, suppresses the transition temperature to 17K, resulting in a metallic state [20]. On the contrary, physical pressure enhances the insulating property of $BaIrO_3$ [21]. This disparate behaviour was also observed in rare-earth (Eu, Gd) doping studies at the Ba site [22]. Zhao et al. grew a series of $BaIr_{1-x}Mn_xO_3$ samples and found structural changes with increasing Mn doping, finally obtaining the 2H form of

BaMnO$_3$ (x = 1). Substituting Mn ions for Ir ions gradually reduces the weak ferromagnetism, resulting in a spin-glass-like behaviour at higher doping concentrations. On the application of pressure, these doped samples assume 6H and 5H forms at different doping levels, revealing properties different from that of undoped 6H and 5H forms of BaIrO$_3$ [23]. Higher doping concentrations of Co at Ir site results in hexagonal structures giving rise to properties like spin glass [24]. All these results demonstrate the sensitive ground state of BaIrO$_3$ and that the electrical and magnetic properties are strongly coupled to lattice degrees of freedom. Drawing motivation from these studies, we decided to investigate the effect of doping a divalent cation at Ba site and study how it effects the J$_{\text{eff}} = \frac{1}{2}$ ground state.

In the present work, we began with Mg doping at the Ba site; during the course of this work we observed that Mg prefers going into Ir site rather than Ba. Thus we shifted our attention to doping Mg at the Ir site and study the structural, magnetic, and transport properties of the resulting compounds. Higher concentrations of Mg-doped samples resulted in change in structure, leading to the formation of a triple perovskite Ba$_3$MgIr$_2$O$_9$ or Ba3129 phase. We made efforts to synthesize samples with lower dopant (Mg) levels; however, most of them seemed to have various amounts of 9R-BaIrO$_3$ and other phases. Electronic and magnetic properties of BaIrO$_3$ and few doped samples have been studied. We also investigated the structural stability of some of the synthesized samples upon heating above room temperature.

The rest of the thesis is structured as follows. A brief structural detail and interactions in iridates are given. Various experimental techniques and methods used in this work have been explained, followed by results and discussion. We conclude the thesis by summarizing the work and prospects of this study.

1.2 The Perovskite Structure

Perovskites are a family of compounds with general formula is ABX$_3$, where A and B are cations of different sizes (the size of the former is greater than the latter), and X is an anion. These compounds get their name from the mineral, perovskite (CaTiO$_3$). Perovskite oxides (ABO$_3$) can accommodate various cations on both A (12-coordinated) and B (6-coordinated) sites. Perovskite structure can be understood as stacks of AO$_3$ layers with B cations in the interlayer holes. In other words, it is built up of corner-sharing or face sharing BO$_6$ octahedra

depending on whether the stacking of layers is cubic close packing (ccp) or hexagonal close packing (hcp) respectively. In addition to these, there are compounds like Na_2IrO_3 that has edge sharing octahedra. Structures with a mixture of hcp and ccp sequence are also possible. The Goldschmidt tolerance factor (t) determines the possibility of the formation of a specific structure.

$$t = \frac{r_A + r_O}{\sqrt{2(r_B + r_O)}}$$

r_A, r_B and r_O are the ionic radii of cations and oxygen respectively

If t = 1, the structure is cubic that consists of corner-sharing BO_6 octahedra. Most of the systems have structural distortions such as tetrahedral distortions, octahedral rotations that deviate them from the ideal cubic structure, resulting in lower symmetries (t < 1) like orthorhombic, tetragonal, etc. [25].

Here we will focus on the structure of $BaIrO_3$ (and its polytypes), which is our subject of interest. As stated earlier, upon the application of high pressure, $BaIrO_3$ exhibits various structural transitions; 9R-6H-5H-3C. The structure of the ambient phase, 9R $BaIrO_3$ is monoclinic (space group C2/m). Here the number 9 represents number of layers and the letter R (rhombohedral) denotes the symmetry. It is named 9R as it is isostructural to 9R-$BaRuO_3$ with a slight monoclinic distortion. It consists of face sharing trioctahedra forming Ir_3O_{12} trimers that are linked to each other by vertices to form columns parallel to the c-axis [15]. These trimers are slightly tilted at an angle of 12° relative to each other. In other words, the structure can be explained as stacking of layers of corner-sharing (C) and face-sharing (F) IrO_6 octahedra in the sequence CFFCFF shown in Fig. 1.3a.

(a) Stacking sequence of BaIrO$_3$ [15]

(b) Ir$_3$O$_{12}$ trimers [16]
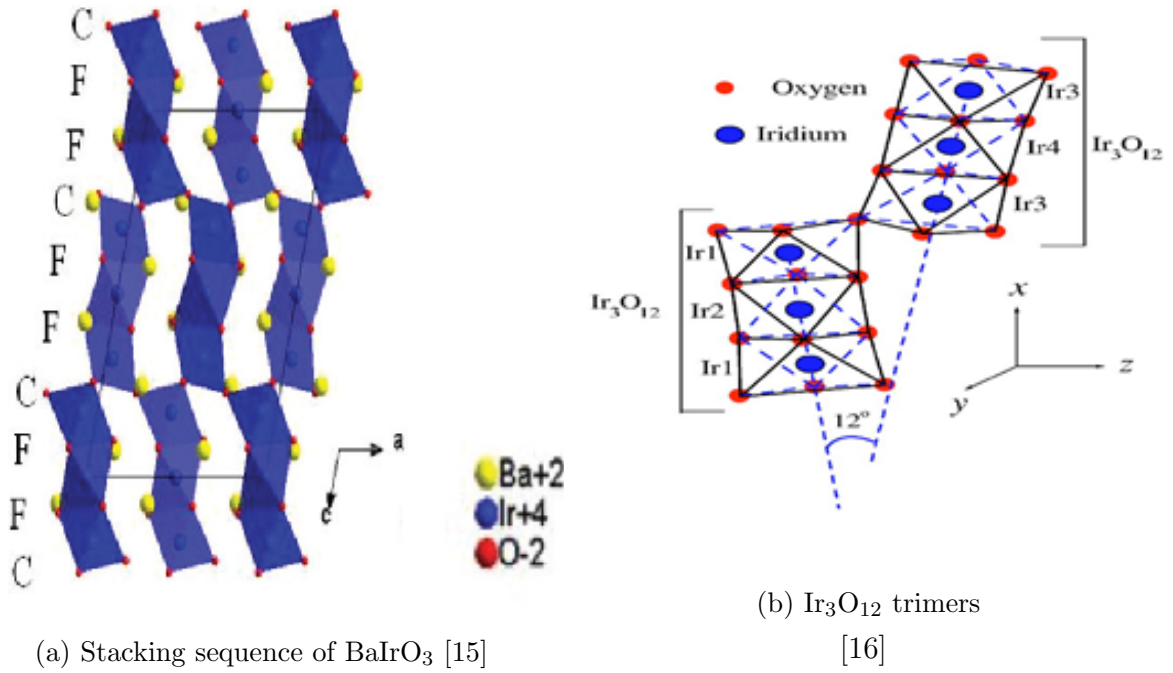
Figure 1.3: Crystal structure of BaIrO$_3$

The 5H polytype crystallizes in the C2/m space group. It contains double Ir$_2$O$_9$ dimers of face sharing IrO$_6$ octahedra. These chains of dimer units are connected via oxygen atoms. In the 6H polytype (C2/c space group), the Ir$_2$O$_9$ dimer units are separated by a single IrO$_6$ octahedron. The 3C phase, which is also the end member of polytypes, has corner-sharing IrO$_6$ octahedra but has a tetragonal structure (*I4*/mcm space group) instead of a simple cubic structure as observed in high-pressure phases of BaRuO$_3$. However, such a tetragonal distortion is typical of an A^{2+}B^{4+}O$_3$ perovskite with a tolerance factor, little less than one [15]. The stacking sequence of layers of corner-sharing (C) and face-sharing (F) IrO$_6$ octahedra in these phases is shown in Fig. 1.4.
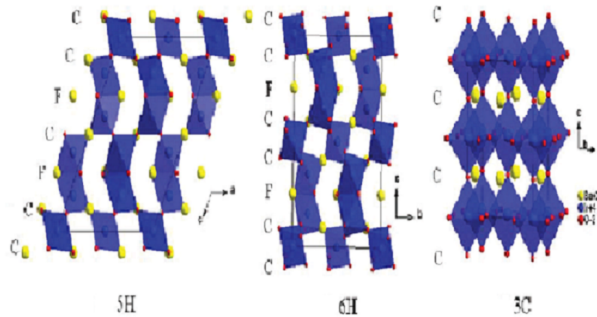

Figure 1.4: Crystal structures of various polytypes of BaIrO$_3$

11

1.3 Interactions

This section gives a brief description of fundamental interactions whose delicate interplay brings out intriguing properties in iridates. As one goes down the the periodic table, $3d \longrightarrow 4d \longrightarrow 5d$, the relative strengths of these interactions changes [see Table 2.1]. These trends are explained in the subsequent sections.

S. No.	Electron type	U (eV)	λ(eV)	Interactions
1	3d	5-7	0.01-0.1	$U > \Delta > \lambda$
2	4d	0.5-3	0.5-3	$U \sim \Delta > \lambda$
3	5d	0.4-2	0.1-1	$U \sim \Delta \sim \lambda$

Table 1.2: Comparison of U, λ and Δbetween 3d, 4d and 5d electrons
[4]

1.3.1 Electronic correlation:

The interaction between the itinerant electrons present in a system is called electronic correlation. Due to the itinerancy of electrons, the system should be conducting and the electrons are delocalised. These electrons can hop from one site to another site, provided the final site is either empty or singly occupied with a spin antiparallel to the incoming electron. However, electrons are not always delocalised. At times, the on-site electrostatic repulsion (U) between the electrons is too high that their pairing energy is enormous. As U increases, hopping reduces and electrons become more and more localised and less metallic. In such cases, the system behaves like an insulator, even though it is predicted to be metallic by the band theory of solids. This is because electron-electron interactions are not considered in conventional band theories. Such systems are called Mott insulators. In a theoretical calculation of the energy of these electrons, within the Hartree – Fock approximation, Coulomb interactions are not taken into consideration. Hence the Hartree-Fock energies obtained for Mott insulators

differ from the actual energies. The difference between the actual and Hartree-Fock energies is called correlation energy. More the difference, more the on-site Coulomb repulsion (U). U decreases, as one goes down the periodic table, from 3d to 5d transition metal ions. This is because the diffused nature of 5d orbitals allow better overlapping relative to 3d orbitals.

1.3.2 Crystal field effect:

In a crystal, an electric field generated around any ion by its neighboring ions is called the crystal field. In many perovskite TMOs, the transition metal cation is octahedrally coordinated with oxygen anions, as shown in Fig. 1.5. The electric field due to electrostatic repulsions from these anions lifts the degeneracy of 5d orbitals and splits them into doubly degenerate, e_g (d_{x2-y2}, d_{z2}) and triply degenerate t_{2g} (d_{xy}, d_{zx} and d_{yz}) orbitals. The t_{2g} orbitals point in between the x, y and z axes; hence have lower overlap with p orbitals of oxygen anions compared to e_g orbitals, which point along these axes. For a better understanding, see Fig. 1.6. This leads to the lower energy of t_{2g} orbitals relative to the e_g orbitals. The crystal field effect on energy levels of an atom depends on the symmetry of the local environment. For example, in the presence of a tetrahedral environment, the splitting is such that t_{2g} and e_g orbitals are higher and lower in energy, respectively.
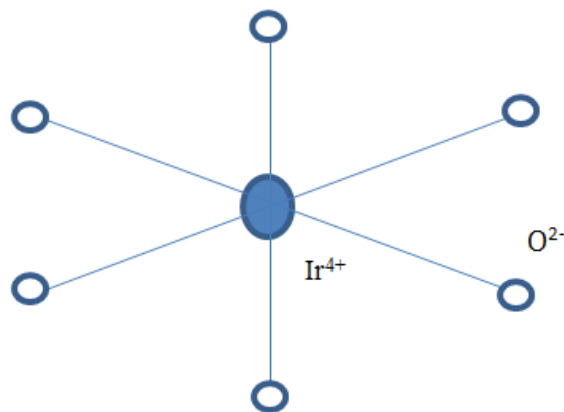
Figure 1.5: Octahedral geometry of transition metal ion
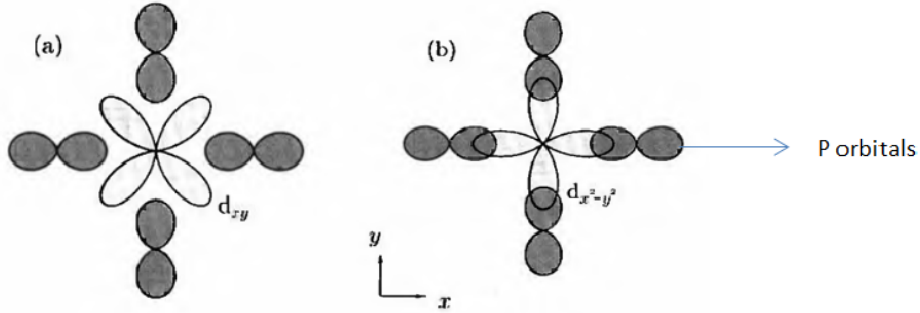
Figure 1.6: Differences in the extent of overlapping
[26]

1.3.3   Spin-orbit coupling:

In an atom, the interaction between the spin and orbital part of the electron's wave function is called spin-orbit interaction(SOC). Consider an electron moving in an atom around the nucleus. The orbital motion of electron generates a magnetic field that interacts with the spin. The spin-orbit interaction energy (λ) scales as Z^4. For 3d elements and their compounds, since they have a relatively lower atomic number, SOC is considered as a weak perturbation. For 5d elements, SOC is strong enough that it is no longer treated as a weak perturbation. For elements with higher Z, the spin and orbital angular momentum of each electron are coupled individually, giving rise to total angular momentum j, of that particular electron, and consequently, the weaker electrostatic effect couples these j values from each electron [26]. This is called j-j coupling.

From the above discussion it is evident that iridates provide a great platform to study the effects of different interactions acting at the same energy scales that would give rise to exciting properties. These novel phenomena in turn provides opportunities for the discovery of functional materials and new devices. Besides a wide variety of physical properties, iridates present a number of challenges that requires in-depth theoretical and experimental investigations.

Chapter 2

Experimental Techniques

2.1 Thermogravimetric analysis:

Thermogravimetric analysis (TGA) is one of the thermal analysis techniques used to examine the change in mass of a substance as a function of temperature or time in a controlled environment. TGA can be used for materials characterization as it provides information about the thermal stability of materials, decomposition patterns, phase transitions, solvent residues. A typical plot of mass or percentage of initial mass vs. temperature or time is called the TGA curve.

A thermogravimetric analyser consists of a sample chamber where a sample pan is located inside a furnace and a balance chamber inside which there is a precision balance. A thermocouple is located to control the temperature accurately. Measurements can be done under various atmospheres like air, vacuum, inert gases, oxidising/reducing gases, controlled pressure. A thermocouple is selected based on the measurement environment and temperature range.

Since MgO is hygroscopic, TGA was done so that weight loss can be accounted in samples' synthesis. The experiment was done using the instrument STA 449 F1 procured from Netzsch. Measurements were done on a MgO sample weighing 12 mg taken in an alumina (Al_2O_3) crucible while maintaining an inert N_2 atmosphere in both sample and balance chambers. The flow rate was maintained at 40 mL/min through the sample chamber and 60

15

mL/min through the balance chamber. An S-type (Platinum-10 % Rhodium) thermocouple was used to monitor the temperature. A heating rate of 10K/min and a temperature range from room temperature up to $900\,^0$C was employed. Utmost care has to be taken while experimenting as the instrument is sensitive to vibrations.

Figure 2.1: TGA setup

2.2   Synthesis

All the samples in this study were synthesized using the conventional solid-state reaction method. It is one of the oldest but effective techniques that is used for synthesizing most of the polycrystalline solids. This method involves the mixing of precursor powders, pressing the mixture into pellets, and heating them at high temperatures such as $1000\,^o$C $-$ $1500\,^o$C. Factors such as melting points of precursors, the temperature of other phase formations (if any) have to be taken into consideration before deciding on sintering temperature.

The precursors used for preparing the parent and doped samples were $BaCO_3$ (Sigma Aldrich, 99.999%), IrO_2 (Sigma Aldrich, 99.9%), MgO (Alfa Aesar, 99.99%). In this study, three series of samples were prepared according to the following set of chemical reactions:

- $BaCO_3 + IrO_2 \longrightarrow BaIrO_3 + CO_2$

- $(1\text{-x})BaIrO_3 + xMgO + xIrO_2 \longrightarrow Ba_{1-x}Mg_xIrO_3$ (x = 0.05)
  $(1\text{-x})\,BaCO_3 + x\,MgO + IrO_2 \longrightarrow Ba_{1-x}Mg_x\,IrO_3 + (1\text{-x})\,CO_2$ (x = 0.1)

- $BaCO_3 + (1\text{-x})\,IrO_2 + x\,MgO \longrightarrow BaIr_{1-x}\,Mg_xO_3 + CO_2$ $(0.05 \le x \le 0.33)$

16

Stoichiometric quantities of precursors were taken and grounded thoroughly in an agate mortar for about 30 minutes. 5% of excess amount of MgO (as determined using the TGA experiment) was taken to account for the weight loss due to its hygroscopic nature as explained in the previous section. The mixed grey powders were placed in an alumina crucible and kept for calcination at 900^oC in the air for 12 hours. Calcination is required for the decomposition of $BaCO_3$ into BaO and CO_2, where CO_2 escapes into the air, and the remaining BaO reacts with IrO_2 and MgO to form the required compound. The calcined black powders were thoroughly ground once again for 30 minutes and pressed into pellets using KBr press. They were sintered at 1000^oC for 24hrs. Two to four such sintering treatments were given depending on the formation of a single phase of each compound.

S. No.	Desired compound	Precursors used	Sintering Temperature	Time of reaction per sintering	No. of sinterings
1	$BaCO_3$	$BaCO_3+IrO_2$	1000^oC	24 hrs	3
2	$Ba_{0.95}Mg_{0.05}IrO_3$	$0.95BaIrO_3 +0.05IrO_2+0.05MgO$	1000^oC	24 hrs	3
3	$Ba_{0.9}Mg_{0.1}IrO_3$	$0.9BaCO_3 +0.05MgO +IrO_2$	1000^oC and 1100^oC	24 hrs	4
4	$BaIr_{0.95}Mg_{0.05}O_3$	$BaCO_3 +0.05MgO +0.95IrO_2$	1000^oC	24 hrs	2
5	$BaIr_{0.9}Mg_{0.1}O_3$	$BaCO_3 +0.1MgO +0.9IrO_2$	1000^oC / O_2 flow	24 hrs	2
6	$BaIr_{0.85}Mg_{0.15}O_3$	$BaCO_3 +0.15MgO +0.85IrO_2$	1000^oC	24 hrs	3
7	$BaIr_{0.8}Mg_{0.2}O_3$	$BaCO_3 +0.2MgO +0.8IrO_2$	1000^oC	24 hrs	3
8	$BaIr_{0.7}Mg_{0.3}O_3$	$BaCO_3 +0.3MgO +0.7IrO_2$	1000^oC	24 hrs	2
9	$BaIr_{0.67}Mg_{0.33}O_3$	$BaCO_3 +0.33MgO +0.67IrO_2$	1000^oC	24 hrs	2

Table 2.1: Sintering conditions of synthesized samples

2.3 Characterisation Techniques

X-Ray Diffraction:

X-ray diffraction is a fundamental characteristic technique to identify the structure of a material, in which a crystalline solid diffracts an incident beam of X-rays. The X-rays produced are made to align in a particular direction by a collimator (a device that produces a parallel beam of rays or radiation). Crystalline solids, due to regular arrangement of atoms behave like a three-dimensional diffraction grating and diffract the incoming x-rays, if the incident wavelength is comparable to the distance between the crystal planes. The scattered waves add constructively satisfying Bragg's law, $n\lambda = 2d\sin\theta$, where, n is the order of diffraction and λ is the incident wavelength of X-rays, d is the spacing between the crystal planes and θ is the angle made by incoming X-rays with the crystal plane.

On heating the filament in the cathode ray tube, electrons are accelerated by a high voltage difference between the anode and the cathode. These electrons transfer a part of their kinetic energy to the anode. When source electrons have enough energy, they remove the inner core electrons of the target material resulting in the formation of a hole. As a result, outer shell electrons move to inner shells to replace the hole. These transitions give rise to the characteristic line spectrum of X-rays. The most intense components of the spectrum, K_α and K_β are the electron transitions from L (n=2) and M (n=3) shells, respectively, to the innermost K (n=1) shell. All the further components of the X-ray spectrum are filtered for getting monochromatic X-rays. The most frequently used target material is Copper (Cu), other materials such as Iron (Fe), Molybdenum (Mo), and Chromium (Cr) are also used. A polycrystalline sample whose crystal planes are orientated in random directions can be used to get information from each set of crystal planes. In order to achieve this randomness, the sample is sometimes rotated. The intensity of scattered waves as a function of diffracting angle (2θ) is obtained. Since the powder diffraction data is unique to each material, xrd acts as a fingerprint for analysing crystal structures.

Powder XRD pattern was obtained for the prepared samples on Bruker D-8 advance X-ray diffractometer in the Bragg-Brentano geometry, using Cu K alpha radiation ($\lambda = 1.5406$ Å). The obtained PXRD pattern was compared with reference patteren available from JCPDS (Joint Committee on Powder Diffraction Standards) database. The 2θ range is maintained from 20° to 80° for all the samples.

19

Figure 2.2: X-ray diffractometer

2.3.1 Scanning Electron Microscopy and Energy Dispersive X-ray Spectroscopy

Scanning Electron Microscopy (SEM) is an electron microscopic technique used to study the morphology and surface features of a compound.

In SEM, a focussed beam of electrons from an electron gun, accelerated through a voltage of 5 - 50 keV are positioned on the sample, where they interact with the sample in various ways. As a result, different particles and radiation arise out of multiple processes. These include secondary electrons (SE), those that are ejected from an atom when bombarded with electrons; back-scattered electrons (BSE), those that are reflected from the sample after elastic scattering without an apparent loss of energy; elastically scattered or diffracted electrons; Auger electrons of characteristic energies; X-rays, both characteristic and white radiation (or Bremsstrahlung); and visible light. In general, any detector can be employed according to the signal of interest that one wants to see. In all SEMs, the Everhart-Thornely detector, a SE and BSE detector is used. It detects these signals; records an image of the sample with the help of the information provided by SE or BSE.

SE are of relatively low energies; hence only those on the surface of the sample reach the detectors. Thus information about the surface features can be known from SE. On the other hand, BSE come from deeper locations of the sample. These are used to see the identity of the elements in a sample. For example, impurity phases can be known.

Energy Dispersive X-ray spectroscopy (EDX) is another characteristic technique used to obtain the elemental composition of a sample. As stated above, one of the radiations obtained due to the interaction of electrons with an atom is characteristic X-rays. When an incident beam excites and ejects an electron from the inner shell of an atom, a hole is created. An electron from the outermost, higher energy shell fills this vacancy. The energy difference between the lower energy shell and the higher energy shell is released in the form of an X-ray that is characteristic of each element. Thus EDX is used for identifying the presence of chemical elements and their abundance.

SEM images and EDX were done on the instrument provided by Zeiss Ultra Plus for all the synthesized samples. Sample preparation for SEM imaging has to be done with utmost care, depending on the size and medium of the synthesized material. As the samples were powder type, they were dry cut into small pellets and affixed on a double-sided conductive carbon tape. This vacuum-compatible carbon tape was, in turn, stuck to an SEM stub. As the samples were highly insulating, to provide a gateway for conduction, they were metal (Au) coated on the surface up to a depth of 8-9 nm. EDS detectors are not reliable for the detection of elements with lighter nuclei. Hence detection of oxygen in the samples was avoided and the relative ratios of Ba, Ir and Mg were taken.

2.3.2   Raman Spectroscopy:

To further characterize the synthesized samples, Raman spectroscopy was done. Raman spectroscopy is a technique used to determine the vibrational modes of a molecule. It operates on the principle of Raman effect, which is the inelastic collision of photons with vibrating molecules of the sample.

When a monochromatic laser beam irradiates a molecule, the scattering is of two types; Rayleigh scattering where most of the scattered light has the same frequency as that of incident radiation (ν_0) and Raman scattering where some part of the scattered light has a frequency (ν_1) different from that of incident radiation. This frequency (ν_1) can sometimes be greater or smaller than that of ν_0; the shift in frequency from $\nu_1 - \nu_0$ is called Raman shift. A typical plot of intensity (I) vs. Raman shift is called the Raman spectrum. Stokes lines appear when energy is absorbed, i.e., the transition from lower to higher energy vibrational level ($\nu_1 > \nu_0$). Anti-stokes lines are observed when energy is emitted, i.e., the transition from

higher to lower energy vibrational level ($\nu_1 < \nu_0$). The symmetry of a sample (molecule) under study also plays a vital role in Raman spectra. For a molecule to exhibit Raman effect, there should be a change in it's polarizability. Raman scattering is a feeble effect; one in a million scattered photons is a Raman photon. Hence a light source that is appropriately focused on the sample, a filter that suppresses the Rayleigh signal, and a sensitive detector to detect the Raman signal are required. In Raman spectroscopy, measurements are done either in 90° or 180° geometries.

All the measurements were done on LabRAM HR provided by Horiba. A Helium-neon or HeNe laser of wavelength 632.8nm was employed as an incident light source. A multi-channel detector: Charge-Coupled Device (CCD) was used as a detector, and an edge filter was used. Measurements were done in back-scattering geometry, where the measured light is the back-scattered light in the direction of the laser. Raman shift range of about $50 - 1000$ cm^{-1} was recorded.
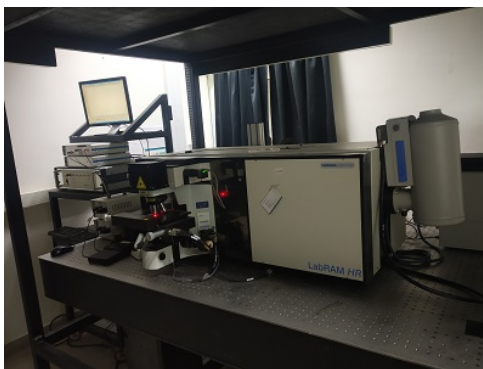
Figure 2.3: Raman spectroscopy setup

2.4   Measurement of Physical Properties:

Measurements of physical properties like resistivity, heat capacity, and susceptibility were performed on single-phase samples using the Evercool II PPMS (Physical Properties Measurements system) by Quantum Design. PPMS can measure properties in a wide temperature range of 1.9K- 400K and magnetic fields up to 9T. PPMS have different probes that facilitate different physical properties measurements. Resistivity, magnetic, and heat capacity measurements were done on synthesized samples that are single phase. Only one option of

the PPMS can be active at a time.

Figure 2.4: PPMS setup

2.4.1 Resistivity Measurements

Electrical resistivity measurements were done by choosing the resistivity option of the PPMS, using the four-probe method. This technique reduces the contribution of contact resistance of leads and the sample resistance can be measured with a greater accuracy. The resistivity sample puck consists of 3 channels; each channel consists of four contact probes. A current (I) is passed through the sample through its current leads and the voltage drop (V) is measured by voltage leads. Resistance (R) is usually measured from Ohm's law, V = IR. Resistance is an extrinsic quantity that depends on the sample size and shape, where as resistivity (ρ) is intrinsic to sample. The resistivity is calculated from the equation,

$$\rho = \frac{V.A}{I.l} \tag{2.1}$$

where A and l are area of cross section perpendicular to the current flow and distance between the voltage leads respectively.

A cigarette paper was attached to the sample puck via GE varnish to prevent the sample from shorting to the puck base. The sample pellet was mounted on the puck using GE varnish for a good thermal contact. One end of each of the gold wires were soldered onto the contact pads while the other end were connected to the sample with silver paint. The contacts were allowed to dry for about two hours in a dry box. A and l of the sample were measured before loading the sample. Resistivity measurements were made between the
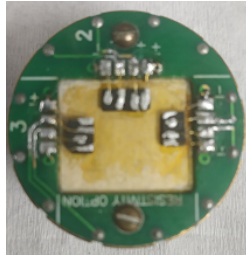
temperature range of 2-300K.

Figure 2.5: Samples mounted on a resisitivity puck

2.4.2 Heat Capacity Measurements

Heat capacity at constant pressure, C_p, i.e $C_p = (dQ/dT)_p$ was measured by selecting the heat capacity option of the PPMS. The basic concept behind heat capacity measurements is that a known amount of energy is added to the sample by heating it in a precise manner, starting from a known temperature, and the corresponding change in temperature is measured. A known amount of heat is applied to the sample at constant power for a fixed amount of time, followed by cooling the sample for the same duration, while the temperature response as a function of time is measured. After every measurement cycle (heating period followed by a cooling period), a mathematical model is used to fit the time dependence of temperature, from which the heat capacity of the sample can be determined. These measurements are carried out in a high vacuum (pressures less than 1mTorr) using the PPMS-High Vacuum option. Such a high vacuum is required to reduce the residual gas, thereby minimizing any heat losses via conduction.

At the beginning of every experiment, a thin layer of Apiezon N grease is applied to the sample platform that is just enough to hold the sample, for good thermal contact between the sample and sample platform. An addenda measurement is done, which is the heat capacity measurement of the sample platform and grease. Care should be taken while mounting the sample on the platform to preserve the exact amount of grease that was put for addenda; else, it will reflect in the accuracy of C_p data. The heat capacity of the sample is then obtained by subtracting the addenda measurement from the total heat capacity (C_p of grease, sample platform and sample). Measurements were done on samples of cross-section 2-3 mm by 2-3 mm and 1mm thickness. The flattest side of the sample was chosen to achieve the best

thermal contact between the sample and the sample platform. If there are any irregularities on the sample, it has to be polished as cracks can impede the thermal contact.
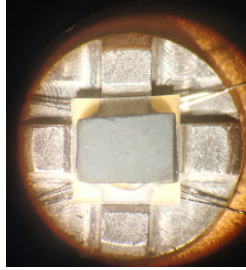

Figure 2.6: Sample pellet mounted on sample holder

2.4.3 Magnetic measurements

Magnetic measurements were made using the VSM (Vibrating Sample Magnetometer) DC magnetometer. The VSM works on the principle of Faraday's law, which states that change in magnetic flux induces a voltage. In VSM, sample is vibrated sinusoidally at a frequency of ~ 40Hz and the induced voltage is measured, which is proportional to the magnetic moment of the sample. The sample was filled in a non-magnetic capillary tube and mounted in a brass holder. The sample holder is such that the region where the sample is placed is uniform throughout. Thus when the sample is vibrated, the vertical displacements of the holder do not create a signal. However, a little imbalance in the positioning of the sample holder will create a signal. The sample was centered in the detection coils using touchdown operation, to prevent these unwanted signals. M vs. T measurements were done in ZFC (Zero field cooling) and FC (Field cooling) mode under 1000Oe in the temperature range of 2-300K. The M vs. H data was taken at 5K.

Chapter 3

$Ba_{1-x}Mg_xIrO_3$ (x = 0, 0.05, 0.1)

In this chapter and the next two chapters, we deal with the structural characterization of synthesized samples based on the results obtained from XRD and FESEM. In the present chapter we present the results of $BaIrO_3$, $Ba_{0.95}Mg_{0.05}IrO_3$ and $Ba_{0.9}Mg_{0.1}IrO_3$. In the next two chapters we discuss the structural characterization of hexagonal perovskites and $BaIr_{1-x}Mg_xO_3$ (x = 0.05, 0.1, 0.15, 0.2). In all these chapters, we first discuss the XRD results, followed by FESEM and EDS analysis. X-ray diffraction patterns of all the samples are compared with the corresponding simulated patterns.

3.1   XRD Analysis

PXRD was obtained for all the synthesized samples. We first present our results of parent compound, $BaIrO_3$, followed by the xrd data of $Ba_{0.95}Mg_{0.05}IrO_3$ and $Ba_{0.9}Mg_{0.1}IrO_3$ samples.

$BaIrO_3$ was analysed by the Rietveld Refinement method using the FullProf program. The diffraction peak profiles were modeled using a psedo-Voigt function while the background was modeled using the linear interpolation method. The Crystallographic Information File (CIF) was obtained from the reference [14]. Fig. 3.1 shows the XRD pattern of $BaIrO_3$ confirming its formation in single phase, crystallising in C2/m space group. The inset table shows values of various goodness of fit parameters. The lattice parameters obtained from the refinement, given in the table 4.1, agrees well with the literature [14].

27
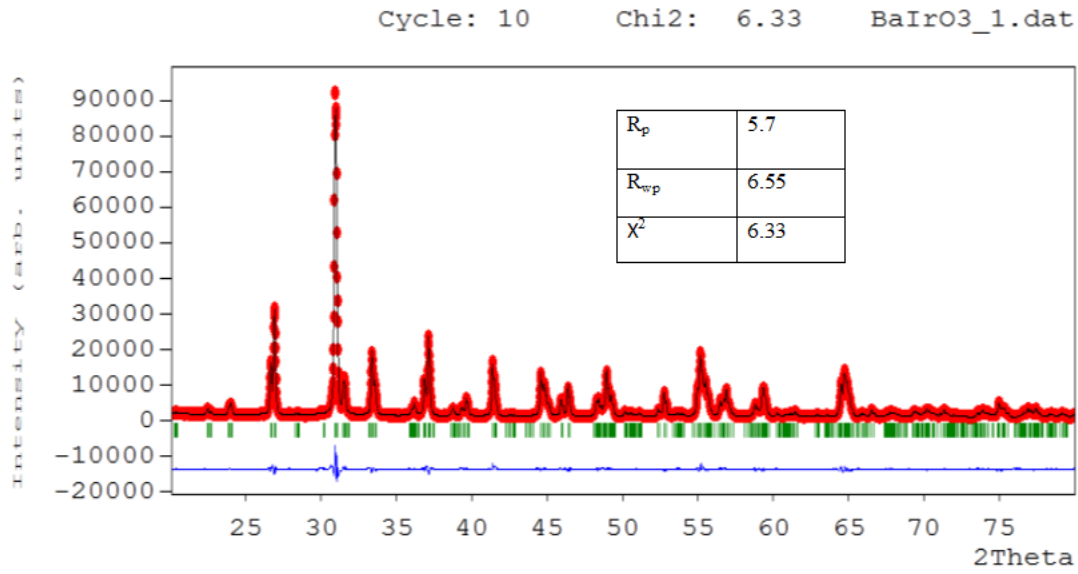
Figure 3.1: Rietveld refined XRD pattern of BaIrO$_3$

Sample	BaIrO$_3$	BaIrO$_3$ (Reported)
a (Å)	10.0053	10.0046
b (Å)	5.75	5.754
c (Å)	15.178	15.184
β	103.272	103.27
Cell Volume (Å^3)	850.19	850.689

Table 3.1: Lattice parameters of BaIrO$_3$

Fig. 3.2 shows the powder x-ray diffraction pattern of the Mg-doped at Ba site samples; $Ba_{0.95}Mg_{0.05}IrO_3$ and $Ba_{0.9}Mg_{0.1}IrO_3$. For the 5% Mg-doped sample, the xrd pattern has a very slight left shift from that of the pure sample, but no new phases were found. In the 10% Mg-doped sample, even after two sinterings, IrO_2 peaks with significant intensity were observed and the peaks due to the main phase were slightly left-shifted contrary to the expectations based on the fact that the ionic radius of Mg^{2+} is significantly smaller than that of Ba^{2+}. The sample was further sintered at a still higher temperature of 1100 ^{o}C, but IrO_2 peaks remained undiminished, indicating that sintering at 1000 ^{o}C or 1100 ^{o}C has no effect on the phase formation. The lattice parameters of the pristine and Mg-doped samples, shown in Table 3.2, indicates that the doping of Mg at Ba site has not affected the lattice significantly in the expected manner. These contradictory observations can, however, be reconciled if one assumes that in these samples, Mg substitutes Ir rather than Ba. The ionic radius of Mg^{2+} (0.72 Å) is comparable to that of Ir^{4+} (0.63 Å), and significantly smaller compared to Ba^{2+} (1.61 Å) [27].
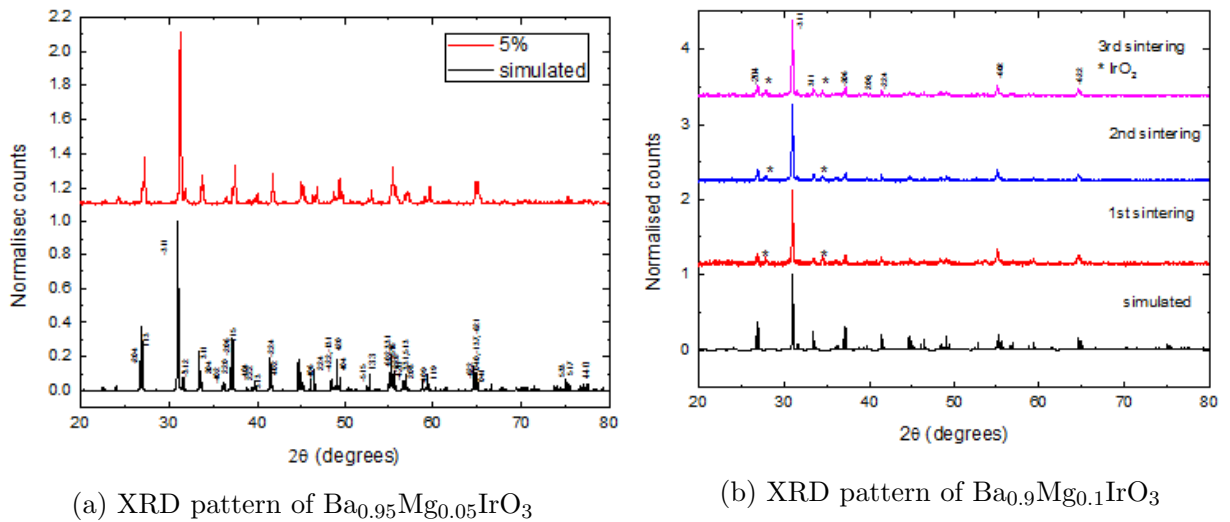

(a) XRD pattern of $Ba_{0.95}Mg_{0.05}IrO_3$

(b) XRD pattern of $Ba_{0.9}Mg_{0.1}IrO_3$

Figure 3.2: XRD patterns of 5 and 10% samples at Ba site

Sample	$Ba_{0.95}Mg_{0.05}IrO_3$	$Ba_{0.9}Mg_{0.1}IrO_3$	$BaIrO_3$
a (Å)	9.9911	9.986	10.0053
b (Å)	5.761	5.76	5.75
c (Å)	15.169	15.145	15.178
β	103.175	103.15	103.272
Cell Volume (Å^3)	850.172	848.27	850.19

Table 3.2: Lattice parameters of doped samples compared with $BaIrO_3$

3.2 FESEM and EDS Analysis

FESEM images and EDS information were obtained to get further insights about the structural characterisation of the samples. Some representative FESEM images are shown in Fig. 3.3. From Fig. 3.3a stacking of layers can be seen for $BaIrO_3$. EDS spectrum was obtained at 7-10 points and the relative ratios were taken. For, $BaIrO_3$ Ba:Ir ratio was 1.01 and for which is in good agreement with the expected value considering the 1-2% instrumental error. In the case of $Ba_{0.95}Mg_{0.05}IrO_3$ (Ba+Mg):Ir ratio was 1.2, which is slightly greater than 1.

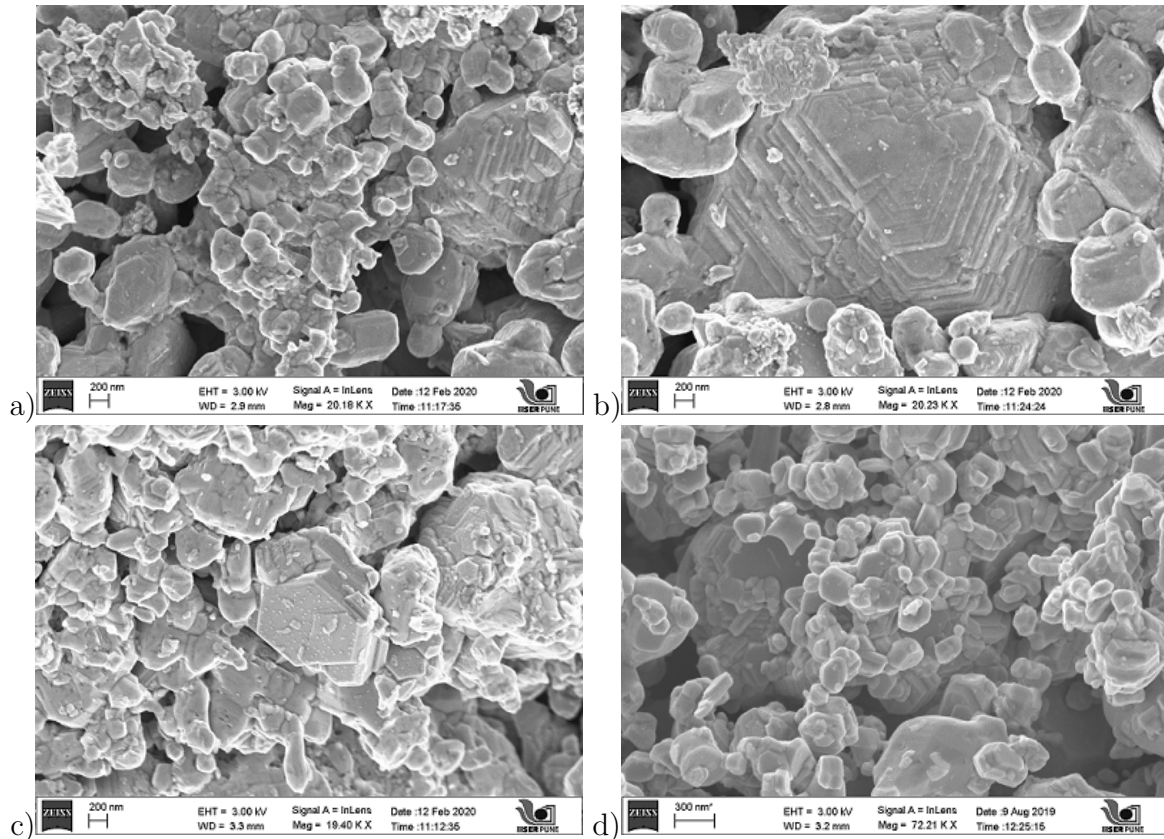Figure 3.3: FESEM images for a) , b) $BaIrO_3$ c)$Ba_{0.95}Mg_{0.05}IrO_3$ and d)$Ba_{0.9}Mg_{0.01}IrO_3$

3.3   Summary

Pristine $BaIrO_3$ was successfully synthesized via solid state method. Efforts were made to dope Mg at the Ba site and we obtained contradictory results since we had expected a considerable decrease in the unit cell volume upon substitution of Ba by smaller Mg; on the contrary, we found that the lattice volume remains nearly unchanged, which suggests that: (i) Mg ions are not incorporated at the Ba-site, and (ii) some of the Mg may have been doped at the Ir site: this scenario is more plausible given that the ionic radius of Mg^{2+} is comparable with that of Ir^{4+}. Given the comparable size of Mg^{2+} ion with Ir^{4+} and its tendency for octahedral coordination, we believe that Mg^{2+} favours going into Ir site rather than Ba Site, which is consistent with the lattice parameters remaining nearly unchanged upon Mg doping.

Chapter 4

Hexagonal Perovskites

After unsuccessful attempts of doping Mg at the Ba site, we decided to synthesize fresh samples by doping Mg at the Ir site in different concentrations and study their properties. It is worth mentioning here that, since we are substituting Mg for Ir, the celebrated $J_{eff} = \frac{1}{2}$ state is no more preserved.

While doping Mg at Ba site, as MgO is hygroscopic, an estimate amount of excess MgO was added. After deciding to pursue doping at Ir site, TGA was done on MgO, resulting in 4.6 % weight loss. Hence 5% excess amount was added to account for the loss.
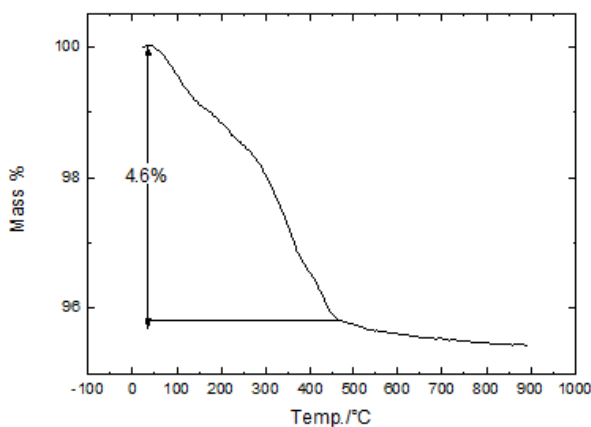
Figure 4.1: TGA curve of MgO

4.1 Structural Characterization

We started with synthesizing higher doping concentration samples; $BaIr_{1-x}Mg_xO_3$ (x = 0.33, 0.3). These samples crystallizes in hexagonal structure (6H) in space group $P6_3/mmc$ [29]. The structural transition from monoclinic to hexagonal is due to the change in the oxidation state of iridium ion from (Ir^{4+}) to (Ir^{5+}) and ($Ir^{4.5+}$) in 33% and 30% samples respectively, as a consequence, size changes from 0.625 Å (Ir^{4+}) to 0.57 Å (Ir^{5+}). The structure consists of two face sharing IrO_6 octahedra forming Ir_2O_9 dimers connected to each other via. vertices of MgO_6 octahedra. The structure in Fig. 4.2 was taken from the reference [41]. Here after, the 33% sample will be referred as Ba3129 phase.
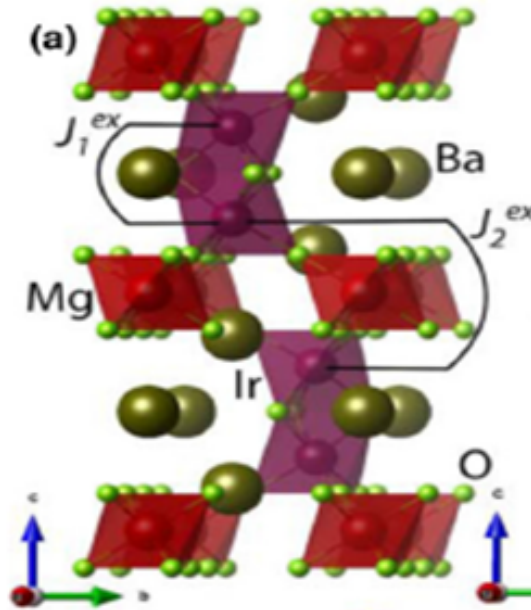

Figure 4.2: Crystal Structure of Ba3129

Fig. 4.3 shows the XRD pattern of 33% sample. The lattice parameters calculated from Unitcell software agree well the literature [29].
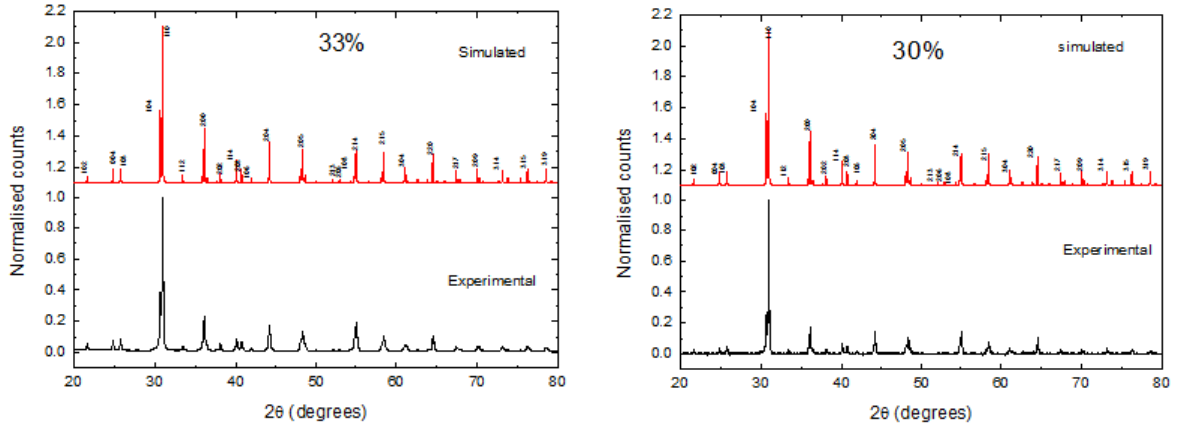
(a) BaIr$_{0.67}$Mg$_{0.33}$O$_3$

(b) BaIr$_{0.7}$Mg$_{0.3}$IrO$_3$

Figure 4.3: XRD patterns of a) 33% and b) 30% samples

Sample	BaIr$_{0.67}$Mg$_{0.33}$O$_3$	BaIr$_{0.7}$Mg$_{0.3}$O$_3$	Ba$_3$MgIr$_2$O$_9$ (Reported)
a (Å)	5.766	5.769	5.772
c (Å)	14.344	14.308	14.321
Cell Volume (Å^3)	412.938	412.376	413.19

Table 4.1: Lattice parameters of 33% and 30% samples

Fig. 4.4 shows the FESEM images of the synthesized samples. Small hexagonal rings can be seen but they are not uniform. From EDS information, the ratio of Ba:(Ir+Mg) was found to be 0.933 and 0.966 for BaIr$_{0.67}$Mg$_{0.33}$O$_3$ and BaIr$_{0.7}$Mg$_{0.3}$O$_3$ respectively, close to the expected value, 1.

35
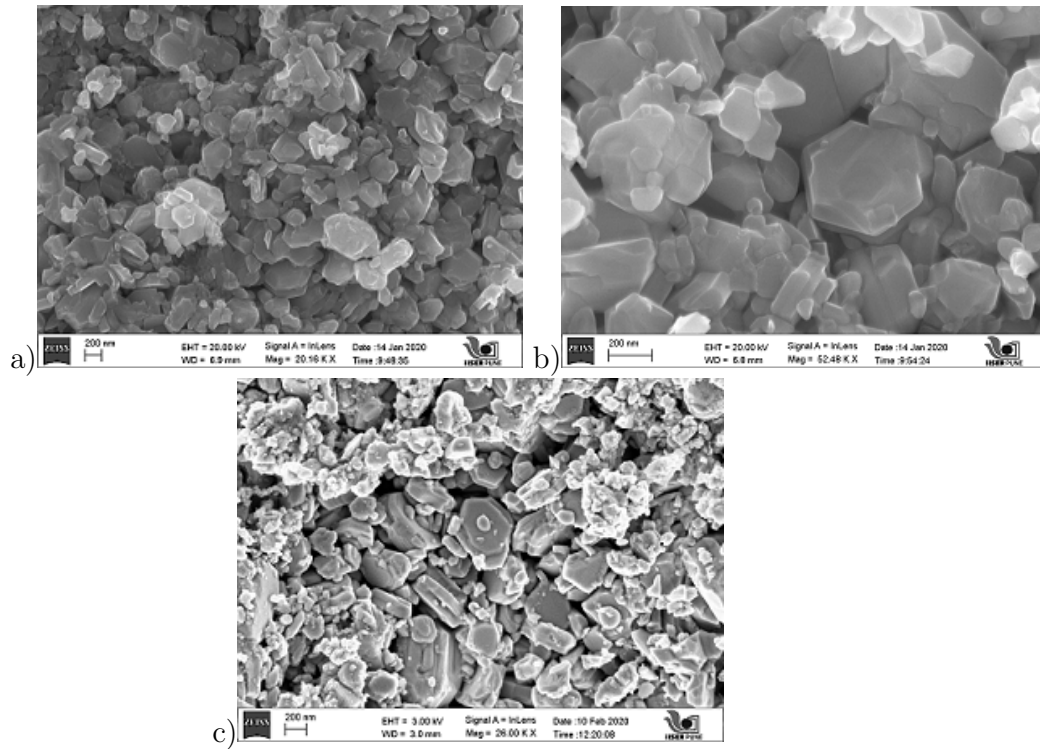
Figure 4.4: FESEM images for a),b)BaIr$_{0.67}$Mg$_{0.33}$O$_3$ and c)BaIr$_{0.7}$Mg$_{0.3}$O$_3$

4.2 Summary

Higher doping levels of Mg at Ir site were successfully synthesized. These samples crystallize with the hexagonal triple perovskite structure. These phases required only 2 sinterings at 1000 ^{o}C, each for 24hrs. On the other hand, studies by Vente et.al [24] reveals that high Co-dopant samples (50%, 70%) required a synthesis period of 14 days for obtaining single phase of hexagonal perovskites. The reason for the ease of formation of Ba3129 phase could be due to the higher tendency of Mg for octahedral coordination.

Chapter 5

$BaIr_{1-x}Mg_xO_3, (x = 0.05, 0.1, 0.15, 0.2)$

We synthesized samples of low dopant(Mg) concentration namely $BaIr_{0.95}Mg_{0.05}O_3$, $BaIr_{0.9}Mg_{0.1}O_3$, $BaIr_{0.85}Mg_{0.15}O_3$, $BaIr_{0.8}Mg_{0.2}O_3$. The 5% sample is found to be completely phase pure within the detection limit of XRD probe (see Fig. 5.1a). For the 10% sample, a small IrO_2 peak was observed. Another batch of the same sample was prepared in oxygen flow, but the IrO_2 persisted. In the case of 15% sample, small rod-like structures were observed in FESEM images [Fig. 5.1f], that corresponds to IrO_2. Fig. 5.1b, shows the XRD pattern of 10% and 15% samples. In the 15% sample, there are additional peaks at $2\theta = 38.2$, 40.2, 40.8, 44.2 and 58.6. Additional peaks are also observed in 10% sample at higher angles ($2\theta = 44.2$, 58.6). It is worth noting that the Ba3129 phase has diffraction peaks around the above mentioned 2θ values [Fig. 5.1c]. The xrd pattern of 20% sample was compared with the simulated pattern of $BaIrO_3$, its high pressure phases and Ba3129 phase [Fig. 5.1d]. The 20% sample seems to be a mixed phase of monoclinic, Ba3129 and the 3C phase. One more observation from the xrd patterns is that the intensity of peaks decreases relative to the highest intensity peak, with increase in Mg concentration, which is depicted in Fig. 5.1e. From EDS analysis, the Ba:(Ir+Mg) ratios for 5% , 10%, 15% and 20% samples are 1.02, 0.95, 1.07 and 0.92 respectively, which are close to the expected value 1 considering the 1-2% instrumental error.

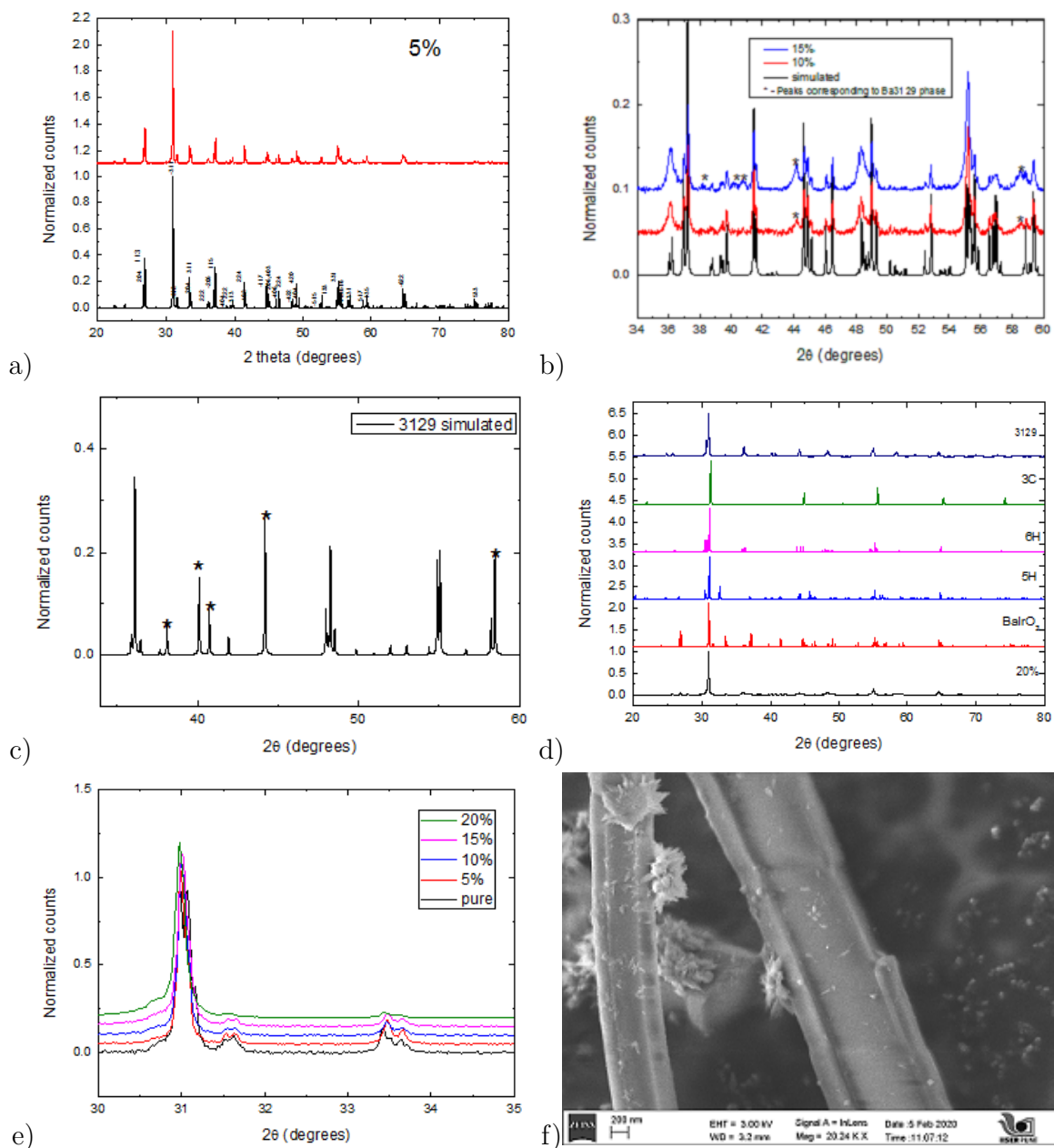Figure 5.1: XRD patterns of 5%, 10%, 15%, 20% and their comparison with other phases. FESEM image of 15% sampls showing rod like structures

An intuitive expectation is that, since the size of Mg^{2+} is greater than Ir^{4+}, as Mg concentration increases, lattice has to expand resulting in increase in cell volume. However; lattice parameters calculated from the Unitcell software did not result in significant change but

there was slight reduction. This is a consequence of partial oxidation of Ir^{4+} to pentavalent iridium, Ir^{5+}. Substitution of one Mg^{2+} results in two Ir^{5+} ions, since the size of Ir^{5+} (0.57 Å) is smaller than Ir^{4+} (0.62 Å), it compensates the expansion of the lattice.

Sample	$BaIr_{0.95}Mg_{0.05}O_3$	$BaIr_{0.9}Mg_{0.1}O_3$	$BaIr_{0.85}Mg_{0.15}O_3$
a (Å)	9.977	9.97	9.99
b (Å)	5.755	5.755	5.754
c (Å)	15.148	15.139	15.149
β(Å)	103.204	103.232	103.23
Cell Volume ($Å^3$)	846.75	845.56	847.28

Table 5.1: Lattice parameters of 5%, 10% and 15% samples

5.0.1 Summary

Except 5% sample, other dopant samples contained parasitic phases. In 10% sample, the parasitic phase corresponds mainly to a small amount of unreacted IrO_2, and a very small concentration of Ba1329. In 15%, the parasitic phase(s) quantity was higher than for the 10% sample. However, the parasitic phases could be identified unambiguously. These observations also agree with doping studies in $SrIrO_3$ by Ilyas Qasim et.al. Their synthetic efforts to dope 3d-transition metal elements at Ir site did not result in a single phase sample at lower concentrations (x $\leq$ 20) [30]. Similarly, Mg doping studies by the same group resulted in mixed phases at low dopant concentrations [31],

Chapter 6

Raman Spectroscopy and HTXRD measurements

To further characterize the samples, Raman Spectroscopy was done. In order to investigate the structural stability of some samples, high-temperature XRD was done. In this chapter, we first present Raman Spectra of synthesized samples followed by HTXRD results.

6.1 Raman Spectroscopy

Raman spectra of the synthesized samples were obtained. Factor group analysis predicts 42 ($25A_g + 17B_1g$) and 19 ($5A_1g + 8E_2g + 6E_1g$) Raman active modes for $BaIrO_3$ and Ba3129 phase respectively [32]. Of these, only 10 modes were observed. One reason for this could be that modes having closely spaced energies are not resolved completely. Fig. 6.1 shows Raman spectra of $BaIrO_3$ and Ba3129. Open circles represent the experimental data and peaks are fitted with Lorentzian function. Corresponding frequencies and full width half maxima (FWHM) were calculated. To the best of our knowledge, Raman spectra of $BaIrO_3$ or Ba3129 phase was not reported in earlier studies. Hence we cannot get the exact frequencies of Raman bands; therefore, we cannot assign vibrational modes. However, we can compare our results with systems having the same space group. We compared our data with $NdLuO_3$, a monoclinic (C2/m) system and $BaTiO_3$, a hexagonal ($P6_3/mmc$) system. [33], [34]. The values are tabulated in table 7.1. It is important to know the origin of various

vibrational modes for a better understanding of doping effect on the spectra. From Fig. 6.1c, it can be seen that as the Mg doping percentage at the Ir site increases, the intensity at $169\,\mathrm{cm}^{-1}$ gradually reduces and completely vanishes for 30% sample. Simultaneously the peak intensity around $750\,\mathrm{cm}^{-1}$ gradually increases from 5% sample and becomes more prominent and highly intense for 33% sample. The reduced mass is inversely proportional to the frequency hence as the reduce mass increases (with increase in Mg doping), the peaks shift towards right. When the Raman spectra of $Ba_{0.95}Mg_{0.05}IrO_3$ and $BaIr_{0.95}Mg_{0.05}O_3$ is compared, an extra peak at $534\ cm^{-1}$ can be seen in the former sample, which is not seen in the latter [Fig. 6.1d]. The reason for this is currently unknown.

Band	BaIrO$_3$	NdLuO$_3$	Ba3129	BaTiO$_3$
1	98.9	96.5	94.81	-
2	107.4	110.5	103.3	106
3	118.3	123.6	125.1	127
4	158.7	168.4	201.6	196
5	170.1	181.1	222.9	218
6	248.3	265	315.1	-
7	311.9	306	360.83	-
8	449.3	440	420	411
9	482.3	486.9	563.5	-
10	601.6	595	749.4	806

Table 6.1: Raman active modes observed in BaIrO$_3$ and Ba3129 phase. (All the frequencies are in cm^{-1}).
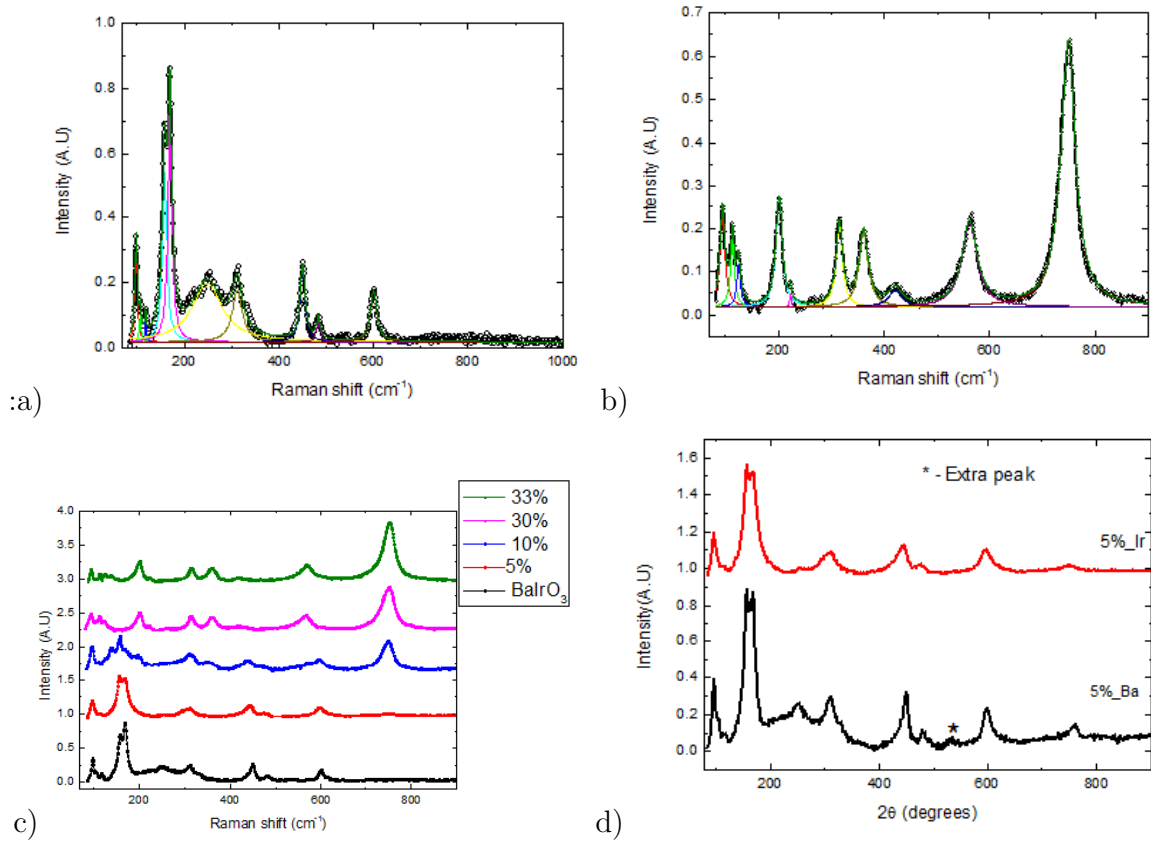
Figure 6.1: Raman spectra of a) BaIrO$_3$ b) 3129 phase

6.2 HTXRD measurements

High temperature XRD measurements were done to see the temperature effect on BaIrO$_3$, BaIr$_{0.95}$Mg$_{0.05}$O$_3$ and Ba3129 samples. A small amount of powdered sample was taken on a Platinum (Pt) plate and was spread uniformly. Since there were no reports on high temperature XRD studies of BaIrO$_3$, we started scanning form 600^oC down to 100^oC. We observed that, at certain 2θ values, two peaks gradually merges into a single peak as temperature increases. This suggests a change in structure. The same was observed in BaIr$_{0.95}$Mg$_{0.05}$O$_3$. In order to make sure that the sructtural changes (if any) are solely due to temperature effect, room temperature (RT) scan was taken before heating and after cooling the samples. These XRD data matches well with the data obtained on normal XRD set up. The diffraction peaks shift slightly towards left due to lattice expansion at high temperature and resumes

43

to their original positions at room temperature. This high temperature XRD did not match with high pressure phases of $BaIrO_3$ or with any of its sister compounds. Crystal structure of the high temperature phase is yet to be known. On the other hand, XRD data obtained at 600^oC for Ba3129 sample did not show any changes except for a slight left shift in peak positions.
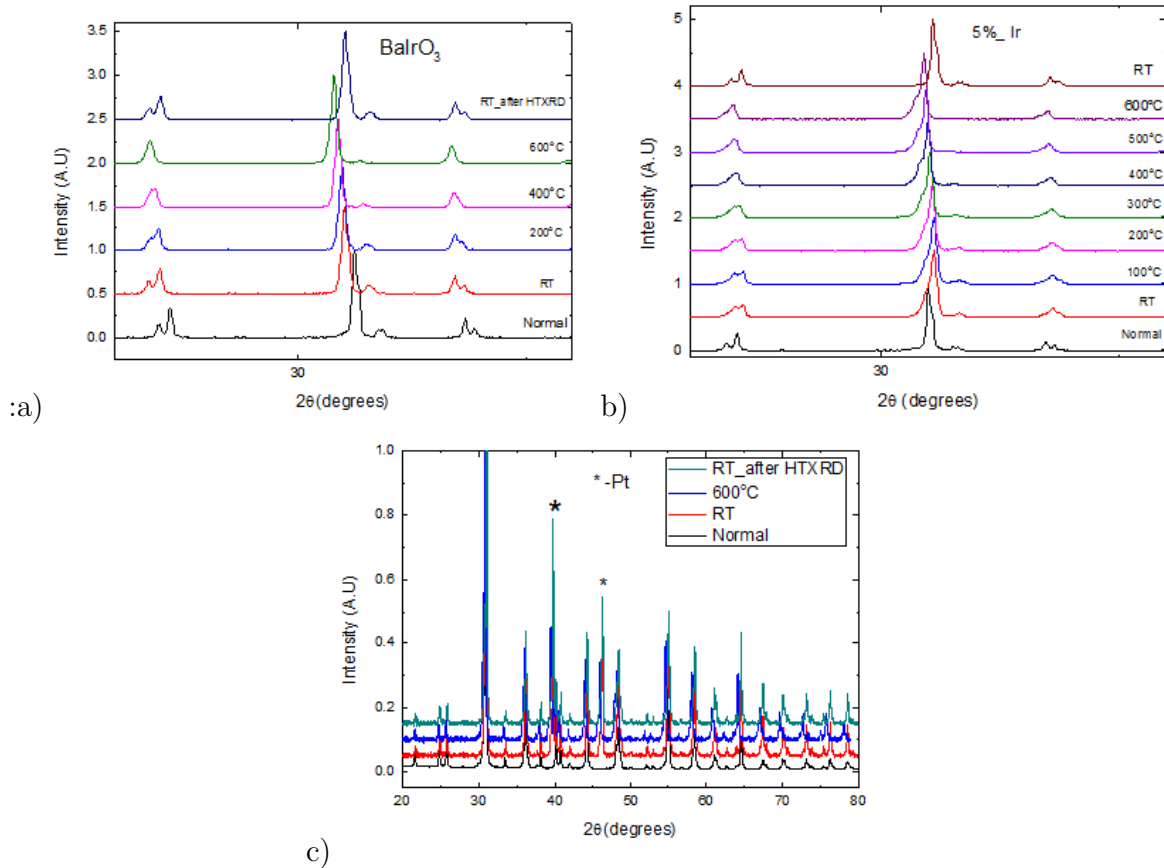
Figure 6.2: HTXRD plots of a) $BaIrO_3$ b) 5%_Ir and c)Ba3129 phase

6.3   Summary

Raman spectra of pristine and doped samples showcases the structural transition supporting XRD results. Insightful information could be drawn from Raman data regarding structural variations and doping. HTXRD suggests a possible change in structure of $BaIrO_3$ at high temperatures between 400^oC and 500^oC. On the other hand, the hexagonal structure of

44

Ba1329 remains stable up to temperatures as high as 600ºC.

Chapter 7

Physical Properties

In this chapter we discuss the physical properties measured for few samples. We first present the results of transport properties, followed by magnetic properties and then specific heat data.

7.1   Transport Properties

We have measured resistivity for three samples; $BaIrO_3$, $Ba_{0.95}Mg_{0.05}IrO_3$ and $BaIr_{0.95}Mg_{0.05}O_3$. Here onwards, we will refer the 5% doped samples at the Ba site and at the Ir site as 5%_Ba and 5%_Ir respectively. Fig. 7.1 shows the resistivity plots of the three samples. For pristine sample, the resistivity decreases with increasing temperature, exhibiting an insulating behaviour. A well defined kink is observed at 184K (a straight line was drawn through the two portion of the resistivity graph where there is a slope change and the point of intersection was considered as the transition temperature) which corresponds to a gap opening due to the formation of a charge-density-wave (CDW) [35]. Different values of transition temperatures (T_c) varying from 173K to 183K were reported by various studies for both polycrystalline and single crystal(SC) samples [34] - [37]. Single crystal studies by G. Cao et al, has reported two more anomalies at 80K and 26K which was not observed here. These anomalies have not been reported in other polycrystalline studies. Between the T_c and 100K, the resistivity increases by a factor of 8, where as studies by Kini et al (Polycrystalline), and G.Cao et al (SC), reported an increase by a factor of 15 and 2 respectively. An increase in magnitude,

upto four orders, is observed below 50K. Reports suggest that lower doping concentrations at Ba site suppresses transition temperature drastically [20], however in our work, T_c seems to have no effect. On the other hand, 5%_Ir sample didn't show any pronounced anomaly. However in $\ln(\rho)$ vs. 1000/T plot, a small change in slope is observed around T_c.

As mentioned before, each Mg^{2+} ion-doped at the Ir site results in doping two holes per formula unit, which increases the hopping probability and hence enhances the electrical conductivity. From Fig. 7.1c, it can be noted that doping at the Ir-site indeed enhances the electrical conductivity and weakens the size of resistivity anomaly. In conventional antiferromagnetic Mott insulators like La_2CuO_4 or NiO, upon hole doping, the electrical conductivity indeed increases while the transition temperature diminishes simultaneously. In $BaIrO_3$, on the other hand, while the size of resistivity anomaly at T_c diminishes, the transition temperature remains nearly unchanged. To compare these two cases further (i.e., hole doping in 3d based Mott insulators, and the unconventional Mott insulating state in 5d TMOs), one should try to introduce holes in the Ir 5d band through doping a monovalent ion directly at the Ir-site, which will be done in future.

In the case of 5%_Ba sample, electrical conductivity has been enhanced, and the size of the resistivity anomaly has diminished relative to the pristine sample but not as much as for the 5%_Ir sample. As mentioned in the earlier chapters, the lattice parameters of the 5%_Ba sample are almost unchanged with respect to the undoped sample, and no extra peaks were detected in the XRD pattern. Based on these observations, we are inclined to conclude that a small fraction of Mg in this sample dopes at the Ir site, which has the same effect as in 5%_Ir sample. Thus, we see behavior that is analogous to 5%_Ir (enhanced electrical conductivity and diminished anomaly) but somewhat diminished due to a lower concentration of Mg at the Ir site. On the other hand, the concentration of remaining Mg that dopes at the Ba site is not large enough to induce an observable lattice contraction. In future, the Rietveld analysis will be performed for this sample to estimate the distribution of doped Mg between the Ba and Ir sites.
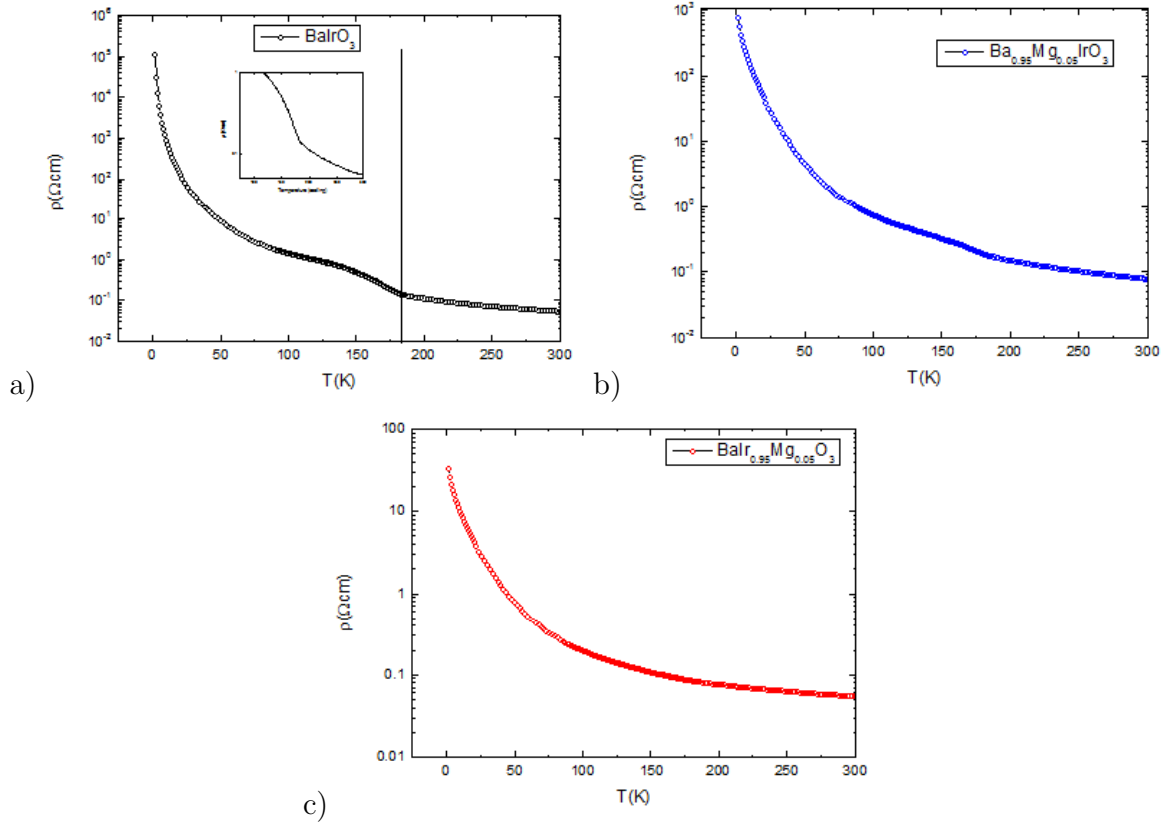
Figure 7.1: Resistivity plots of a) $BaIrO_3$ b)$Ba_{0.95}Mg_{0.05}IrO_3$ and c) $Ba_{0.95}Mg_{0.05}IrO_3$

Resistivity data were fitted with Arrhenius model using the formula, $\rho = \rho_o exp(\Delta/T)$, where Δ is the activation energy. For all the samples, the resistivity above T_c fits best with this model. From the Arrhenius plot, the calculated activation energy is 39.26 meV, which is within the range of reported values, 25 - 50 meV [9]. For 5%_Ba and 5%_Ir samples, the activation energies are 33.45 meV and 16.77 meV respectively.
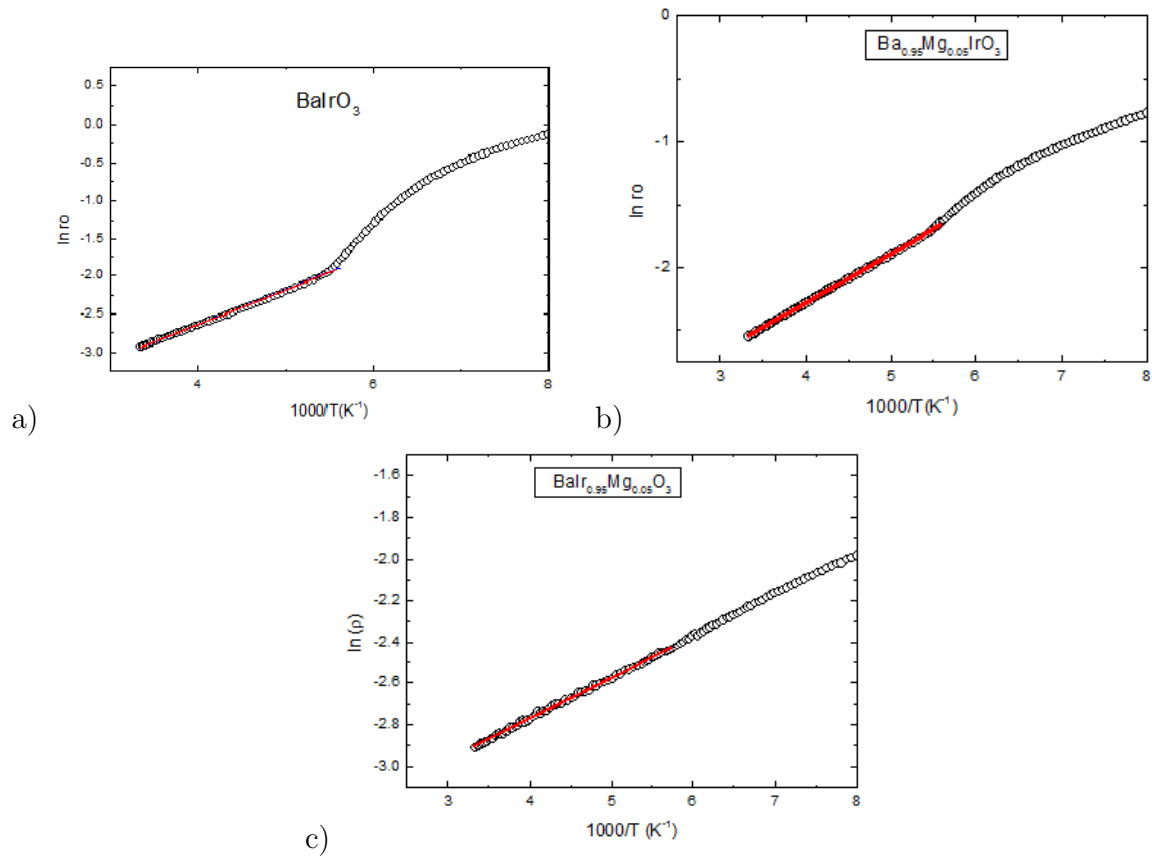
Figure 7.2: Arrhenius plots of resistivity for a) $BaIrO_3$ b)$Ba_{0.95}Mg_{0.05}IrO_3$ and c) $Ba_{0.95}Mg_{0.05}IrO_3$

Fig. 7.3 shows the normalized resistivity plot. All the samples show insulating behaviour throughout the measured temperature range. The order of magnitude in doped samples decreases to a greater extent relative to pure sample.

Figure 7.3: Resistivity data normalized with resistivity at 300K vs. Temperature

50

7.2 Magnetic measurements

We measured the magnetic susceptibility as a function of temperature for pristine, 5%_Ba, 5%_Ir and Ba3129 phase. Fig. 7.4 shows the plot of magnetic susceptibility vs. temperature.

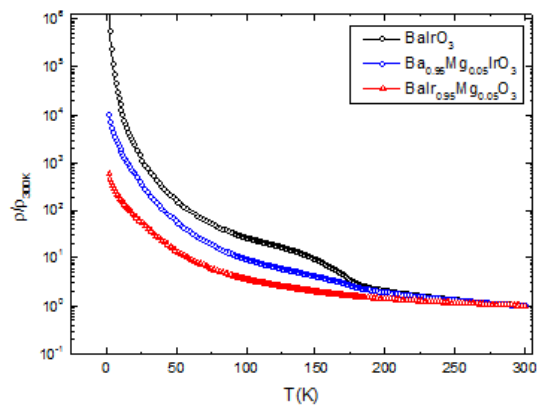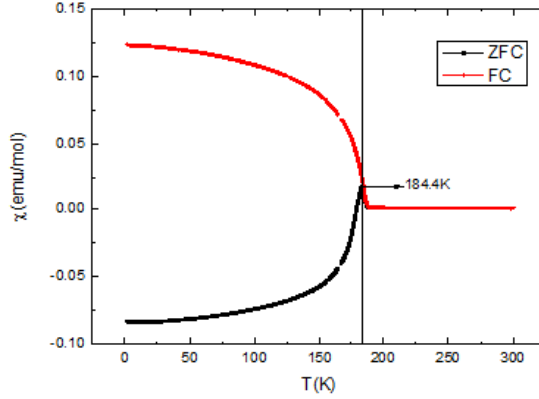Figure 7.4: Magnetic susceptibility data of $BaIrO_3$

The zero-field-cooled (ZFC) curve and the field-cooled (FC) curves separate at 184.4K. A sharp rise of the ZFC susceptibility upon cooling below 184 K is due to the onset of ferromagnetic ordering of the Ir^{4+} moments [18]. The behaviour of ZFC and FC susceptibility are in agreement with the previous reports [35] - [37], but the ferromagnetic ordering temperature is slightly higher than the range of reported values, 175K-183K. In $BaIrO_3$, the ferromagnetic ordering and CDW formation occurs simultaneously at the same temperature. The susceptibility values of χ_{FC} are comparable with those reported in [37]. Fig. 7.5 shows the magnetic susceptibility plots for 5%_Ba and 5%_Ir samples. For both the samples, there is no change in transition temperature in agreement with the electrical resistivity reported in the previous section. In the 5%_Ba sample, the behavior of ZFC-FC, and the magnitude of susceptibility, are in close agreement with undoped $BaIrO_3$. Also, the ZFC susceptibilities are negative for $BaIrO_3$ and 5%_Ba samples. On the other hand, in the 5%_Ir sample, both the ZFC and FC susceptibilities are negative, and their magnitude is much smaller compared to the undoped sample.

Generally, in a ferromagnetic sample, a negative ZFC susceptibility often results when the strength of the applied magnetic field is weaker than the coercive field (H_c) of the

sample (assuming that the remnant field of the magnet, in which the sample is cooled to the lowest temperature, is negative). Since H_c itself depends on temperature (decreases as temperature increases), a smaller applied field (H_a) than the coercive field at the lowest temperature causes the measured susceptibility to remain negative until the sample is heated up to a temperature where H_a overwhelms H_c. However, to throw light on the exact cause of negative susceptibility in these samples, it would be necessary to carry out more detailed magnetic measurements. In particular, it will be useful to do M vs. H measurements at various temperatures below T_c to examine the temperature dependence of H_c.

The high temperature χ vs T data of BaIrO$_3$ and 5%_Ir samples, was fitted to the Curie-Weiss law using the equation, $\chi = \chi_0 + \dfrac{C}{T - \Theta_p}$. Here χ_0 is the temperature independent paramagnetic susceptibility, C is the Curie constant, and Θ_p is the Curie-Weiss temperature. The obtained values of the pristine sample are $\chi_0 = 8.12$ x 10^{-4} emu/mol, C = 0.007 K emu/mol and $\Theta_p = 183$K. The effective magnetic moment, μ_{eff}, calculated from the formula $\sqrt{8C}$ is 0.22 μ_{B}/Ir which is slightly greater than the reported values, 0.13 μ_{B}/Ir and 0.186 μ_{B}/Ir [35], [38]. On the other hand, the Curie constant (C) and the Curie-Weiss temperature (Θ_p) of 5%_Ir are 0.004 K emu/mol and 183K respectively; μ_{eff} is 0.17 μ_{B}/Ir. By comparing the above values for BaIrO$_3$ and 5%_Ir, it can be noted that Mg-doping reduces μ_{eff} while Θ_p remains to be the same.

To summarize, the effect of 5% Mg doping at the Ir site is to weaken the magnetic susceptibility (i.e., reduce the magnitude of χ) without changing the magnetic ordering temperature. The observation of negative χ in both ZFC and FC runs is rather interesting and requires further investigation for a better understanding. On the other hand, in the 5%_Ba sample, though the magnitude of χ has reduced slightly, the overall behavior is analogous to that of BaIrO$_3$, which is in line with our interpretation that Mg does not dope at the Ba site.
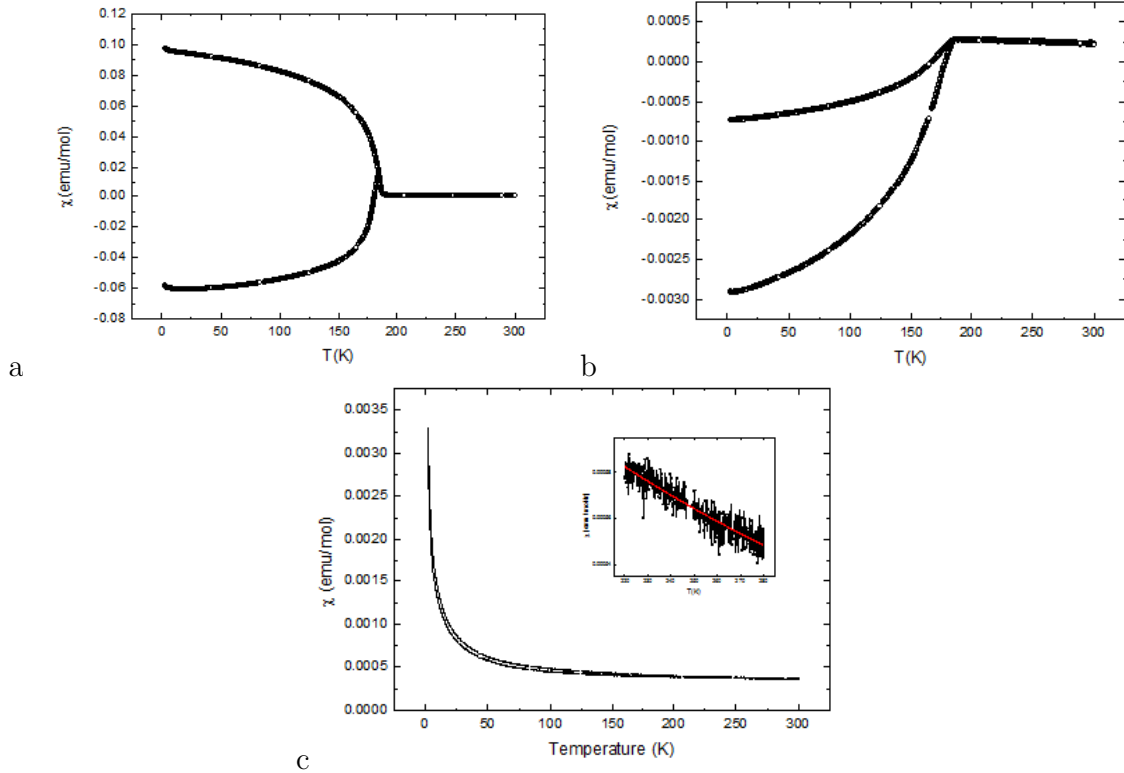
Figure 7.5: Magnetic susceptibility data of a) 5%_Ba b) 5%_Ir and c) Ba3129 phase. The inset of c) shows the Curie-Weiss fitting at high temperature.

The ZFC and FC curves of 33% sample have almost overlapped with each other. However there is a slight opening of the curves below T $\sim$ 200K [Fig. 7.5]. When the high temperature data is fitted with the Curie-Weiss law (inset of Fig. 7.5) , the extracted values of C and Θ_p are 0.12 K emu/mol and -209.78K respectively, although no ordering is seen in the susceptibility data at this temperature, the ZFC-FC curves show a small splitting. The negative value of Weiss-temperature suggests that the effective interactions are antiferromagnetic in nature. The effective magnetic moment is 0.97 μ_B/Ir. Such high μ_{eff} (0.91 μ_B/Ir) and negative Θ_p (-229K) are observed in studies by Cao. et al on Sr_2YIrO_6 [42]. However other studies on Sr_2YIrO_6, have reported much lower values of μ_{eff}; within the range of $\sim$ 0.16 - 0.6 μ_B/Ir [39]. Interestingly, the Curie-Weiss temperature obtained in our work is much smaller than other hexagonal pentavalent iridates whose values lies with in the range of -50K to -20K [41]. What is more intriguing is that systems with Ir^{5+} ions are expected to be non magnetic due to their J = 0 ground state. Ir^{5+} has $5d^4$ configuration, which should

have completely filled t_{2g} orbitals, resulting in a non magnetic ground state. However all the reported pentavalent iridates so far, have exhibited magnetic behaviour defying the common knowledge. Various hypothesis and mechanisms have been proposed to explain these properties which are listed below:[39]

- Initially it was believed that the magnetic ground state is due to the IrO_6 octahedral distortions that creates non cubic crystal fields (crystal field arising out of nonequivalent Ir - O bond lengths). These crystal fields are responsible for partial quenching of orbital angular momentum.

- Excitations between J = 0 and J = 1 states, given the energy of J = 1 is sufficiently small.

- Presence of Ir^{4+} or Ir^{6+} ions in the compound due to off stoichiometry.

- Anti-site disorders (disorder that arises when atoms in a crystal are displaced) might as well contribute to magnetic behaviour. Increased interactions lead to increased overlapping thereby reducing orbital angular momentum.

Laguna-Marco et al, [39] in their recent studies have revisited Sr_2YIrO_6 and explained its magnetic behaviour using a combination of various experimental techniques. Their studies showcase that magnetism in this compound (which, in earlier studies was attributed to structural distortions) is due to the presence of Ir^{4+} or Ir^{6+} ions. We believe same is the case with our system, but it is just a crude estimation and needs a detailed study.

To throw light on this issue, further studies are required on samples prepared with intentional Mg-Ir offstoichiometry. It is for this reason that the 30% sample was prepared. However, due to lack of time on the magnetometer, such studies could not be completed on time. But in future we plan to carry out a systematic magnetization study on samples with Mg : Ir ratio slightly off from its ideal value.

7.3 Specific heat measurements

We measured the specific heat capacity for pristine, 5%_Ba, 5%_Ir and hexagonal structures. An anomaly around the T_c has been observed agreeing with susceptibility data. The anomaly

is rather broad and is barely distinguishable from the phononic background when plotted over the whole temperature range. The values of specific heat are comparable with the reported values but the anomaly at T_c in our samples is rather broad compared to the single crystal samples reported previously [35], [18]. At low temperatures the lattice contribution to the specific heat varies according to C $\propto T^3$ law while metals have an additional term γT due to electrons. To know the low temperature (T $\leq$ 10K) behaviour of the sample, C/T vs. T^2 was plotted and the data was fitted using the equation C/T $= \gamma + \beta T^2$. Here γ and β are electronic and phononic contribution to the specific heat respectively. By obtaining the slope (β) of C/T vs. T^2 plot, Debye temperature can be calculated using the formula,

$$\Theta_D = \left(\frac{12\pi^4 nR}{5\beta}\right)^{1/3}$$. Here n = number of atoms present in a formula unit, R = universal gas constant, β = phononic contribution to specific heat.

The calculated Deye temperature and γ for our undoped $BaIrO_3$ sample is 219K and 2.21 mJ/K^2 in agreement with previous reports [35], [38].
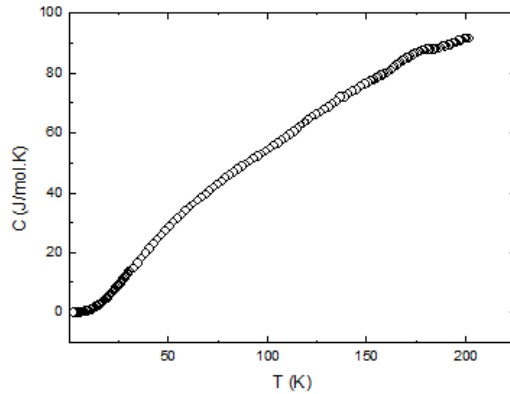

Figure 7.6: Specific heat of $BaIrO_3$

Fig. 7.7 shows the specific heat data of doped samples. The kink near T_c is observed only in 5%_Ba sample which is also observed in resistivity and susceptibility data. In the 5%_Ir sample no discernible anomaly could be observed, which is likely due to the weakening of the magnetic ordering as inferred from the resistivity behavior also. Other doped samples similarly do not show any anomaly throughout the temperature range. From C/T vs. T^2 plots it can be noted that there is a slight upturn below 2.5K and 3.7k for 30% and 33% samples. Such a low temperature upturn below 2.5K was observed in MnBi single crystals

(space group $P6_3/mmc$) but the reason was not known [40]. Further studies are required to know the underlying mechanism of low-temperature behaviour.
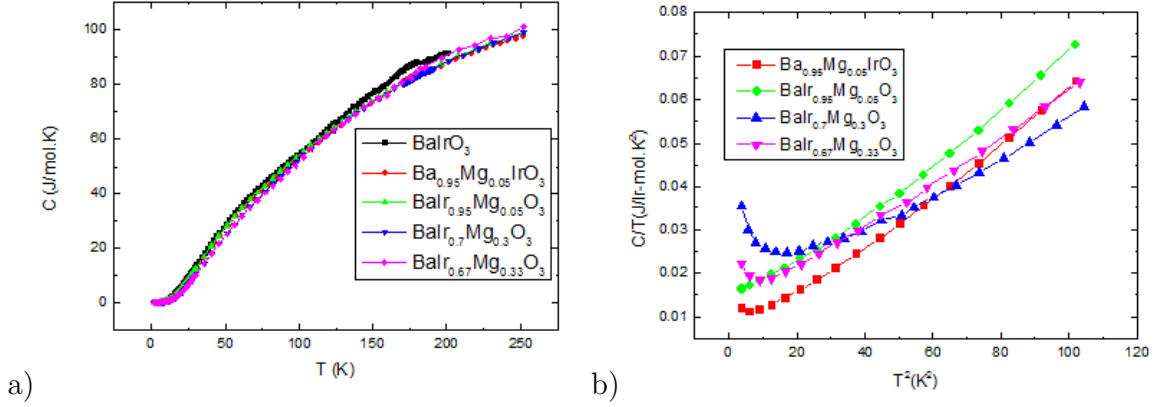

Figure 7.7: Comparison of specific heat data

7.4 Summary

Physical properties of BaIrO$_3$, 5%_Ba, 5%_Ir and hexagonal phases were studied. Properties of BaIrO$_3$ agree well with the literature. At this point we can compare the structure and physical properties of 5%_Ba and 5%_Ir samples. Based on the powder X-ray diffraction results, we can conclude that these samples crystallize in monoclinic (C2/m) space group as that of the undoped BaIrO$_3$ sample. However, from the variation of unit cell parameters, we conclude that Mg-doping at the Ba-site is highly unlikely. On the other hand, due to its favorable size and choice of octahedral coordination, Mg-dopes readily at the Ir-site. Physical properties of these two samples, and their comparison with the undoped BaIrO$_3$, reveals that the insulating ground state of BaIrO$_3$ is rather sensitive. The electrical resistivity decreases by several orders by doping merely 5% Mg at the Ir site, but the magnetic ordering temperature remains unchanged upon doping. However, the size of the anomalies in resistivity and specific heat reduces significantly upon doping of Mg at the Ir site. Whether this is due to suppression of CDW or due to weakening of the ordered Ir magnetic moment is not yet clear and should be investigated further. Such behaviour is also corroborated by Zhao et al, [23], where only 5% doping of Mn is responsible for the disappearance of the kink in the specific heat. The Ba3129 phase shows magnetic behaviour despite having a non-magnetic ground state. A low temperature upturn in specific heat is observed for 30% and Ba3129 phase.

Chapter 8

Conclusion and Outlook

We have successfully synthesized $BaIrO_3$ and a series of doped samples. The phase purity and compositions of these samples were analyzed using powder X-ray diffraction, FESEM and Raman spectroscopy. Our initial efforts of doping Mg at the Ba site were unsuccessful. On the other hand, we found that Mg dopes Ir readily due to its favorable size and preference for an octahedral coordination. The monoclinic phase was retained up to 5% Mg doping at the Ir site but the higher Mg concentration samples (10%, 15% and 20% doping) were found to be in mixed phase consisting mainly of the 9R monoclinic phase of the parent $BaIrO_3$, and the hexagonal triple perovskite phase of $Ba_3MgIr_2O_9$. However, on the $Ba_3MgIr_2O_9$ end of the phase diagram, we found that reducing the Mg concentration from 33% to 30%, retains the hexagonal structure. The study of solid solubility between Mg and Ir at this end of the phase diagram is planned for future studies. These samples will be very useful in shedding light on the outstanding issue of Ir^{5+} magnetism, which has attracted considerable attention recently. Currently Rietveld refinement is being done for 10%, 15% and 20% samples to know the amount of different phases present in these intermediate compositions; thereby, we can obtain a complete structural phase diagram with increasing Mg concentration. Theoretical calculations are needed to assign vibrational modes in Raman spectra which will be done in future.

Physical properties have been measured on the single phase samples. We find that doping Mg at the Ir site results in significant decrease in the electrical resistivity but the magnetic ordering temperature remains unchanged. Since, $Ba_3MgIr_2O_9$ is highly insulating, it would

be interesting to see how the electrical conductivity varies across the series. To this end, as mentioned above, we plan to investigate the magnetic behavior of samples with Mg : Ir stoichiometry slightly off from the ideal value of 1 : 2. Given numerous explanations for the origin of magnetism in pentavalent iridates, it will be interesting to know the underlying mechanism for magnetic behaviour in these samples. Analogous to chemical pressure, heating the sample above room temperature also has an effect on the structural stability of $BaIrO_3$. Currently, we are trying to find the crystal structure of high temperature phase of $BaIrO_3$. In future, we plan to grow samples of much higher concentrations ($> 33\%$) to see if the triple perovskite structure persists or it assumes structures with higher symmetry.

Bibliography

[1] M. K. Wu, J. R. Ashburn, and C. J. Torng , Superconductivity at 93 K in a New Mixed-Phase Y-Ba-Cu- O Compound System at Ambient Pressure, *Physical Review Letters. 58 (9): 908–910*, (1987).

[2] G.H . Jonker, J.H. Van Santen , Ferromagnetic compounds of manganeese with perovskite structure, *Physica. 16 (3): 337*, (1950).

[3] G. Cao and Lance E. DeLong, Frontiers of 4d- and 5d- Transition Metal Oxides Gang Cao and Lance E. DeLong, *World Scientific Publishing Company*, (2013)

[4] Gang Cao and Pedro Schlottmann , The challenge of spin–orbit-tuned ground states in iridates: a key issues review, *Rep. Prog. Phys. 81 042502*, (2018)

[5] J. P. Clancy, N. Chen, C. Y. Kim, W. F. Chen, K. W., Plumb, B. C., Jeon, T. W. Noh, and Y. Kim, Spin-orbit coupling in iridium-based 5 d compounds probed by x-ray absorption spectroscopy, *Phys. Rev. B, vol. 86, no. 19, pp. 1–8*,(2012).

[6] William Witczak-Krempa, Gang Chen, Yong Baek Kim, and Leon Balents. Correlated quantum phenomena in the strong spin-orbit regime. *Annu. Rev. Condens. Matter Phys., 5(1):57-*,(2014).

[7] Kim B J et al., Novel Jeff = Mott state induced by relativistic spin-orbit coupling in Sr_2IrO_4, *Phys. Rev. Lett* ,(2008).

[8] Ding Y et al, Pressure-induced confined metal from the mott insulator $Sr_3Ir_2O_7$, *Phys.Rev.Lett 116216402*, (2016).

[9] Weiwei Ju, Guo-Qiang Liu and Zhongqin Yang, Exotic spin-orbital Mott insulating states in $BaIrO_3$, *Phys. Rev.B 87,075112*, (2013).

[10] Okabe, H., Isobe, M., Takayama- Muromachi, E., Koda, A., Takeshita, S., Hiraishi, M., Miyazaki, M., Kadono, R., Miyake, Y., and Akimistu, J., Ba_2IrO_4: a spin-orbit Mott insulating quasi- two –dimensional antiferromagnet, *Phys Rev. B 83155118*, (2011).

[11] Longo JM, Kafalas JA, Arnott RJ. Structure and properties of the high and low pressure forms of $SrIrO_3$. *J Solid State Chem ;3:174–9*, (1971).

[12] Sarkozy RF, Moller CW, Chamberland BL , The characterization of calcium iridium oxides, *J. Solid State Chem ;9:242-6*, (1974).

[13] Ohgushi K, Yagi T, Gotou H, Kiuchi Y, Ueda Y., Metallization of quasi-two-dimensional Mott insulator CaIrO$_3$ with S = 1/2 spins, *Physica B ;404:3261–3*,(2004).

[14] Cheng JG, Alonso JA, Suard E, Zhou JS, Goodenough JB, A New Perovskite Polytype in the High- Pressure Sequence of BaIrO$_3$, *J Am Chem Soc 131:7461–9*, (2013).

[15] Cheng JG, Zhou JS, Alonso JA, Goodenough JB, Sui Y, Matsubayashi K, Uwatoko Y., High-pressure synthesis of the BaIrO$_3$ perovskite: A Pauli paramagnetic metal with a Fermi liquid ground state, *Phys Rev B ;80:104430*, (2009).

[16] Kalobaran Maiti, Electronic structure of BaIrO$_3$: A first-principles study using the local spin density approximation, *PHYSICAL REVIEW B 73, 115119*, (2006).

[17] Yunqi Cai, Yan Li and Jinguang Cheng, 'Synthesis, Crystal Structure, and Physical Properties of the Perovskite Iridates' in Perovskite materials : synthesis, characterisation, properties, and applications. InTech, Rijek, Croatic, pp 185-218, (2016).

[18] Cao G, Crow JE, Guertin RP, Henning PF, Homes CC, Strongin M, Basov DN, Lochner E. , Charge density wave formation accompanying ferromagnetic ordering in quasi-one-dimensional BaIrO$_3$, *Solid State Comm ;113:657–62*, (2000).

[19] Brooks ML, Blundell SJ, Lancaster T, Hayes W, Pratt FL, Frampton PPC, Battle PD, Unconventional magnetic properties of the weakly ferromagnetic metal BaIrO$_3$, *PhysRev B ;71:220411(R)*, (2005)

[20] Cao G, Lin XN, Chikara S, Durairaj V, Elhami E., High-temperature weak ferromagnetism on the verge of a metallic state: Impact of dilute Sr doping on BaIrO$_3$, *Phys Rev B; 69:1744118*,(2004).

[21] M. A. Laguna-Marco, G. Fabbris, N. M. Souza-Neto, S. Chikara, J. S. Schilling, G. Cao,and D. Haskel, Different response of transport and magnetic properties of BaIrO$_3$ to chemical and physical pressure, *PHYSICAL REVIEW B 90, 014419*,(2014).

[22] Korneta OB, Chikara S, Parkin S, DeLong LE, Schlottmann P, Cao G. , Pressure-induced insulating state in Ba$_{1-x}$R$_x$IrO$_3$ (R=Gd,Eu) single crystals, *Phys Rev B;81:045101*, (2010).

[23] J.G. Zhao , L.X.Yang , Y.Yu, F.Y.Li , R.C.Yu , C.Q.Jin , Structural and physical properties evolution of BaIr$_{1-x}$Mn$_x$O$_3$ solid solutions synthesized by high-pressure sintering, *Journal of Solid State Chemistry 183, 720–726*, (2010).

[24] Jaap F. Vente and Peter D. Battle, Structural Chemistry and Electronic Properties of the Hexagonal Perovskites BaIr$_{1-x}$Co$_x$O$_3$ (x = 0.5, 0.7, 0.8), *Journal of Solid State Chemistry 152, 361-373*,(2000).

[25] Richard J. D. Tilley, Perovskites - Structure-property relationships,Chichester: Wiley,(2016).

[26] S.Blundell and D. Thouless, Magnetism in condensed matter. Vol. 18. Oxford: Oxford university press, (2001).

[27] R. D. SHANNON, Revised Effective Ionic Radii and Systematic Studies of Interatomie Distances in Halides and Chaleogenides, *Acta Cryst. A32, 751*, (1976).

[28] TJB Holland and SAT Redfern, Unit cell refinement from powder diffraction data: the use of regression diagnostics, *Mineralogical Magazine, 61(404):65–77,*(1997).

[29] Takeshi Sakamoto, Yoshihiro Doi, Yukio Hinatsu, Crystal structures and magnetic properties of 6H-perovskite-type oxides $Ba_3MIr_2O_9$ (M = Mg, Ca, Sc, Ti, Zn, Sr, Zr, Cd and In), *Journal of Solid State Chemistry 179 2595–2601*, (2006).

[30] Ilyas Qasim, Brendan J. Kennedy and Maxim Avdeev, Synthesis, structures and properties of transition metal doped $SrIrO_3$, *J. Mater. Chem. A, 1, 3127*, (2013).

[31] Ilyas Qasim, Brendan J. Kennedy and Maxim Avdeev, Stabilising the orthorhombic perovskite structure in $SrIrO_3$ through chemical doping. Synthesis, structure and magnetic properties of $SrIr_{1-x}Mg_xO_3$ ($0.20 \leq$ x ≤ 0.33), *J. Mater. Chem. A, 1, 13357*, (2013).

[32] E. Kroumova, M. I. Aroyo, J. M. Perez Mato, A. Kirov, C. Capillas, S. Ivantchev H. Wondratschek, Bilbao Crystallographic Server: useful databases and tools for phase transitions studies, *Phase Transitions 76, Nos. 1-2, 155-170* (2003).

[33] Júlia C. Soares, Kisla P.F. Siqueira , Roberto L. Moreira , Anderson Dias, Structural and vibrational properties of phase-pure monoclinic $NdLuO_3$ interlanthanides synthesized from nanostructured precursors, *Journal of Alloys and Compounds 678, 57-64*, (2016).

[34] Hirotaka YAMAGUCHI, Hiromoto UWE, Tunetaro SAKUDO and Etsuro SAWAGUCHI, Raman Scattering Study of the Soft Phonon Modes in Hexagonal Barium Titanate, *Journal of the Physical Society of Japan , Vol 56, No.2, pp. 589-595*, (1987)

[35] N.S. Kini, A. Bentien, S. Ramakrishnan, C. Geibel, Specific heat and transport study of the co-existence of charge-density-wave and weak ferromagnetism in BaIrO3, *Physica B 359–361, 1264–1266*, (2005).

[36] Ichiro Terasaki et al, Novel Charge Ordering in the Trimer Iridium Oxide $BaIrO_3$, *Crystals, 6(3), 27*, (2016).

[37] Tomohito Nakano and Ichiro Terasaki, Giant nonlinear conduction and thyristor-like negative differential resistance in $BaIrO_3$ single crystals, *PHYSICAL REVIEW B 73, 195106*, (2006).

[38] J.-G. Cheng, J.-S. Zhou, J. A. Alonso, J. B. Goodenough, Y. Sui, K. Matsubayashi, and Y. Uwatoko , Transition from a weak ferromagnetic insulator to an exchange-enhanced paramagnetic metal in the $BaIrO_3$ polytypes, *PHYSICAL REVIEW B 80, 104430,* (2009).

[39] M. A. Laguna-Marco et al, Magnetism of Ir^{5+} based double perovskites: Unraveling its nature and the influence of structure, *PHYSICAL REVIEW B 101, 014449,* (2020).

[40] Michael A. McGuire, Huibo Cao, Bryan C. Chakoumakos and Brian C. Sales, Symmetry-lowering lattice distortion at the spin-reorientation in MnBi single crystals, *Phys. Rev. B 90, 174425,* (2014).

[41] Abhishek Nag et al, $Ba_3MIr_2O_9$ hexagonal perovskites in the light of spin-orbit coupling and local structural distortions, *PHYSICAL REVIEW B 97, 064408,* (2018).

[42] G. Cao, T. F. Qi, L. Li,1 J. Terzic, S. J. Yuan, L. E. DeLong, G. Murthy, and R. K. Kaul, Novel Magnetism of Ir^{5+} ($5d^4$ Ions in the Double Perovskite Sr_2YIrO_6, *PRL 112, 056402,* (2014).